

# **Inverse modeling of methane sources and sinks using the adjoint of a global transport model**

Sander Houweling,<sup>1</sup> Thomas Kaminski,<sup>2</sup> Frank Dentener,<sup>1</sup> Jos Lelieveld,<sup>1</sup> and Martin Heimann<sup>3</sup>

Short title: INVERSE MODELING OF METHANE

---

<sup>1</sup>Institute for Marine and Atmospheric Research Utrecht (IMAU), Utrecht University, The Netherlands.

<sup>2</sup>Max Planck Institute of Meteorology, Hamburg, Germany.

<sup>3</sup>Max Planck Institute of Bio Geo-chemical Cycles, Jena, Germany.

**Abstract.** An inverse modeling method is presented to evaluate the sources and sinks of atmospheric methane. An adjoint version of a global transport model has been used to estimate these fluxes at a relatively high spatial and temporal resolution. Measurements from 34 monitoring stations and 11 locations along two ship cruises by the National Oceanographic and Atmospheric Administration have been used as input. Recent estimates of methane sources, including a number of minor ones, have been used as a priori constraints. For the target period 1993–1995 our inversion reduces the a priori assumed global methane emissions of 528 to 505 Tg(CH<sub>4</sub>) yr<sup>-1</sup> a posteriori. Further, the relative contribution of the Northern Hemispheric sources decreases from 77% a priori to 67% a posteriori. In addition to making the emission estimate more consistent with the measurements, the inversion helps to reduce the uncertainties in the sources. Uncertainty reductions vary from 75% on the global scale to ~1% on the grid-scale (8°x10°), indicating that the grid scale variability is not resolved by the measurements. Large scale features such as the interhemispheric methane concentration gradient are relatively well resolved and therefore impose strong constraints on the estimated fluxes. The capability of the model to reproduce this gradient is critically dependent on the accuracy at which the interhemispheric tracer exchange and the large-scale hydroxyl radical distribution are represented. As a consequence, the inversion-derived emission estimates are sensitive to errors in the transport model and the calculated hydroxyl radical distribution. In fact, a considerable contribution of these model errors cannot be ignored. This underscores that source quantification by inverse modeling is limited by the extent to which the rate of interhemispheric transport and the hydroxyl radical distribution can be validated. We show that the use of temporal and spatial correlations of emissions may significantly improve our results; however, at present the experimental support for such correlations is lacking. Our results further indicate that uncertainty reductions reported in previous inverse studies of methane have been overestimated.

## 1. Introduction

Our understanding of atmospheric methane is to a large extent limited by a poor quantification of its sources. Although the dominant methane-producing processes seem to be identified, their global distributions as well as globally integrated source strengths are still highly uncertain. Some sources for which relatively reliable statistics exist, for instance, emissions by domestic ruminants, are relatively well constrained by integrating or scaling-up the sources. For sources that have a large natural variability, for example, emissions from rice paddies and natural wetlands, the opposite is true. Despite considerable effort to constrain these important sources, progress is slow. For example, the amount of methane released from rice paddies has recently been estimated at  $80 \pm 50 \text{ Tg}(\text{CH}_4) \text{ yr}^{-1}$  [Lelieveld *et al.*, 1998], indicating an uncertainty range similar to the IPCC [1990] estimate of nearly a decade ago (20–150 Tg(CH<sub>4</sub>)/yr). Recent estimates of global methane emissions from natural wetlands, the largest single source of methane, by Lelieveld *et al.* [1998] and Hein *et al.* [1997] disagree strangely ( $145 \pm 30$  and  $232 \pm 27 \text{ Tg}(\text{CH}_4) \text{ yr}^{-1}$ , respectively).

Measurements over the past decade show a significant variability of the globally averaged methane trend. The fluctuations in the early 1990s have been merely attributed to the Mount Pinatubo eruption, but the underlying processes remain unclear [Dlugokencky *et al.*, 1994a, 1996]. Recent measurements indicate that the methane trend continues to decline [Dlugokencky *et al.*, 1998]. For the changes observed so far the sources and sinks of methane are not well enough constrained to provide a reliable explanation. As a consequence, the foundation for any future scenario of methane in the atmosphere is weak. It is important to improve our understanding of the atmospheric budget of methane since it plays an important role in radiative and chemical balances in the atmosphere.

In addition to upscaling techniques, inverse modeling can be used to estimate sources. This method makes use of measurements of trace gas concentrations, which are translated to constraints on the sources by means of an atmospheric transport model. Generally, the number of available measurements is a limiting factor in this approach. For such an inverse problem

to have a single solution either the number of emission parameters to be estimated must be adjusted according to the available measurements, or different constraints must be introduced. Often it is required that the solution be close to existing knowledge by introducing first guess or a priori information of the sources. This can be done in a consistent way by adopting a so-called Bayesian approach, in which all parameters are expressed as statistical probability distributions. A solution in the form of a superposition of all statistical distributions involved can be computed, from which means and covariances can be derived.

Until now a number of studies have quantified global-scale sources using inverse methods aiming at different trace gases, such as CFCs [*Brown, 1993; Hartley and Prinn, 1993; Plumb and Zheng, 1996; Mulquiney and Norton, 1998; Mulquiney et al., 1998*], CH<sub>4</sub> [*Brown, 1993, 1995; Hein et al., 1997*], CO<sub>2</sub> [*Enting et al., 1995; Rayner et al., 1996; Law and Simmonds, 1996; Kaminski et al., 1999b*]. In all these studies except the last, fluxes are aggregated into a few large regions. This “big region” approach has the disadvantage that emission distributions over predefined regions are assumed to be perfectly well known, which, in practice, is justified by computational limitations rather than by knowledge about the sources. In fact, such an approach may lead to significant biases in the estimated emissions caused by nonhomogeneous sampling by the measurement network as shown by *Tramper and Snieder [1996]*. Presently, it is unknown at which resolution fluxes should be represented in order to reduce this bias to an insignificant size. Sensitivity studies, however, show that significant biases occur when continental-scale regions are applied (T. Kaminski, personal communication, 1998).

The aim of this paper is to study the sources and sinks of methane on a global scale and to assess the usefulness of the existing measurement data as constraints. In this study, as opposed to previous studies, biases are minimized using the method of *Kaminski et al. [1999a]*. To compute efficiently the large number of sensitivities needed to perform an inversion in this approach, an adjoint model is used. Except for the definition of the fluxes and the method to derive the sensitivities the method we adopt resembles the method by *Hein et al. [1997]*.

Compared with this study, the measurements and first-guess assumptions have been extended and updated.

Using our method, the inverse problem is strongly underdetermined because of the large increase in the number of unknown compared with *Hein et al.* [1997], whereas the number of constraints (measurements) is about the same. This can be interpreted as a reduction of a priori information since temporal and spatial distributions of the sources and sinks within the regions are no longer assumed to be well known. In fact, we choose the opposite starting point by assuming that the uncertainties in the fluxes are fully uncorrelated. From this viewpoint the big region approach can be considered as a case in which all fluxes over a region are assumed to be fully correlated. Hence our confidence in the a priori emission distributions can be expressed in the spatial and temporal correlation of source and sink uncertainties. Our method allows different scenarios for treating these correlations.

In the next section the inverse modeling technique will be explained. We describe the model in section 3, a priori knowledge on sources and sinks and measurements in sections 4 and 5, and the relevant chemistry in section 6. In section 7 the results of the methane inversion are presented, focusing on differences between a priori and a posteriori estimates. The impact of correlated uncertainties is studied in section 8, where we also present results using different scenarios. Sensitivity tests have been performed to investigate the potential influence of the major assumptions on the estimated sources and sinks. Finally, the ability of this method to solve questions related to different emissions scenarios has been studied with rice paddies as a test case in section 9.

## **2. Inversion Method and Unknowns**

To deduce information about surface emissions from measured concentrations, we use a global atmospheric chemistry transport model (CTM) that relates these emissions to concentrations. In mathematical terminology the CTM defines a mapping (or function) of a parameter set (including the emissions) on the simulated concentrations. For any measured

methane concentration  $d_{i,t}$  at location  $i$  and month  $t$  this function can be written in the form

$$d_{i,t} = d_{i,t}[\mathbf{f}, \mathbf{Q}(\mathbf{f}, s_{OH}, s_{stra}, c_0), \mathbf{R}(\mathbf{f}, s_{oh}, s_{stra}, c_0), c_0], \quad (1)$$

where any component  $f_{j,m}$  of the vector  $\mathbf{f}$  represents the integrated surface emission over region  $j$  and month  $m$ . Since  $f_{j,m}$  may either represent a surface source or sink, in the following the term “flux” will be used to denote exchange between the surface and the atmosphere. The  $s_{OH}$  parameterizes the chemical removal of methane  $\mathbf{Q}$  due to the reaction with the hydroxyl radical in each tropospheric grid box. Similarly,  $s_{stra}$  and  $\mathbf{R}$  refer to stratospheric methane loss as a result of the reactions with  $O(^1D)$ , Cl, Br, OH radicals, and methane photolysis. Finally,  $c_0$  is defined as the global mean methane concentration at the start of a simulation. The aim of the inversion is to find the set of most probable values for the parameters  $\mathbf{f}$ ,  $s_{OH}$ ,  $s_{stra}$ , and  $c_0$ . For this purpose we iteratively apply a linear inversion procedure that combines the set of observations  $d$  and a set of a priori estimates  $\tilde{\mathbf{f}}$ ,  $\tilde{s}_{OH}$ ,  $\tilde{s}_{stra}$ , and  $\tilde{c}_0$  using (1).

We need to iterate because the chemistry introduces a nonlinearity as explained below. The amount of methane  $Q_{k,l}$  oxidized by hydroxyl radicals in a particular tropospheric grid box  $k$  and month  $l$  can be represented as

$$Q_{k,l} = s_{OH} k_{OH}(T) [OH]_{k,l} [CH_4]_{k,l}, \quad (2)$$

where  $k_{OH}$  is the temperature-dependent rate constant for the reaction between the hydroxyl radical and methane. The dependency of the amount of methane oxidized on its concentration  $[CH_4]_{k,l}$  causes a nonlinear response to the fluxes at the observational sites. Since tropospheric methane oxidation influences the hydroxyl radical concentration, there is also a feedback mechanism through changes of  $[OH]_{k,l}$ . Similar nonlinearities occur because of the stratospheric sink.

Different strategies can be adopted to define the fluxes represented by the parameters  $f_{j,m}$ . One approach is to classify fluxes geographically, for example, per continent or country [see, e.g., *Hartley and Prinn* [1993]; *Mulquiney et al.* [1998]]. Alternatively, a classification

distinguishing different flux-producing processes can be used, as is done, for instance, by *Hein et al.* [1997]. Unless both the emission distributions over the specified regions and the model are perfect, non homogeneous sampling by the sparse network will lead to biased emission estimates [*Trampert and Snieder*, 1996]. This bias can be reduced by decreasing the size of the regions or by defining the regions such that the uncertainty in the flux distribution over each region is minimal. Because of the large spatial variability of CH<sub>4</sub> emissions, we lack such well-defined regions. Therefore, over the continents we choose to represent the surface flux in every continental surface grid box of our CTM by a separate flux parameter. In contrast, ocean grid boxes without linkages to continents or continental shelves are aggregated into one single region. For all fluxes, including those from the oceans, a temporal resolution of 1 month is used; hence seasonal cycles are also subject to optimization.

The open ocean source is mainly driven by a small methane supersaturation in the surface layer, ranging from 0.95 to 1.17 over the oceans [*Bates et al.*, 1996]. Although the methane concentration in ocean water has been determined at a limited number of sites only, the available data suggest that the net emission is only small and that the variability is not large enough to influence significantly the atmospheric methane concentration distribution. The north and south polar ice shields are treated similarly to the oceans, which is justified by the absence of any known significant surface source or sink in these regions. As a result of both flux aggregations, the total number of surface flux parameters is reduced by about a factor of 2.

In (2) we scale the amount of methane oxidized in every tropospheric grid box by a single parameter  $s_{OH}$ , which implies that the entire spatiotemporal distribution of the OH radical field is kept constant. Unlike the ocean and polar sources, such a treatment of the OH sink is not sustained by our knowledge of the tropospheric OH distribution. Treating the OH sink this way is equivalent to assuming that the OH distribution is perfectly known, which is not the case. In fact, we lack the tools to validate model-simulated OH distributions for aspects other than large-scale averages. The fact that other reactive trace gases, such as carbon monoxide

and ozone, are simulated realistically by our model [*Houweling et al.*, 1998] indicates, however, that the large-scale chemistry and transport are adequately represented. Therefore we fix the OH distribution, assuring that the optimized methane flux fields are consistent with our knowledge of global tropospheric chemistry. We return to this discussion in section 6.

For the stratospheric sink we used a fixed spatiotemporal CH<sub>4</sub> loss distribution derived from the two-dimensional (2-D) chemistry transport model of *Brühl and Crutzen* [1993] since our CTM does not have an accurate representation of the stratosphere. The error introduced by this method is expected to be small as it appears that surface methane concentrations are relatively insensitive to changes in this distribution because of the relatively long exchange time between the troposphere and stratosphere. Formally, the stratospheric sink also introduces a nonlinearity. Since the CH<sub>4</sub> loss distribution has been fixed, the feedback of the methane concentration on stratospheric oxidation is neglected, which eliminates this nonlinearity.

The linearized form of (1), including the simplifications as discussed above, is represented by

$$\begin{aligned}
 d_{i,t} = & \Delta c_0 + \sum_{j,m} \frac{\partial d_{i,t}}{\partial f_{j,m}} \Delta f_{j,m} - \frac{\partial d_{i,t}}{\partial s_{stra}} \Delta s_{stra} \\
 & - \sum_{k,l} \frac{\partial d_{i,t}}{\partial Q_{k,l}} \left( \sum_{k,l} \frac{\partial Q_{k,l}}{\partial [CH_4]_{k,l}} \Delta [CH_4]_{k,l} + \frac{\partial Q_{k,l}}{\partial s_{OH}} \Delta s_{OH} \right) \\
 & + d_{i,t} [\tilde{\mathbf{f}}, Q([\tilde{CH}_4], \tilde{s}_{OH}), \tilde{s}_{stra}, \tilde{c}_0],
 \end{aligned} \tag{3}$$

where the tilde designates a first-guess estimate. In general, the relative changes in the CH<sub>4</sub> concentration resulting from the inversion-derived changes in the fluxes are small (<5%), so that the term  $\frac{\partial Q_{k,l}}{\partial [CH_4]_{k,l}} \Delta [CH_4]_{k,l}$  in (3) can be neglected. In a second iteration of the inversion procedure the changes in  $[CH_4]_{k,l}$  are taken into account by linearizing around the improved values for  $\mathbf{f}, s_{OH}, s_{stra}$  and  $c_0$ . Generally, after the second iteration the changes in the results have become insignificant (<1%).

In vector notation, (3) can be formulated as

$$\Delta \mathbf{d} = \mathbf{T} \Delta \mathbf{f} - \mathbf{S} \Delta \mathbf{s} + \Delta c_0, \tag{4}$$

where  $\mathbf{s}$  includes both  $s_{OH}$  and  $s_{stra}$ . The Jacobian matrix  $\mathbf{T}$  contains concentration responses to the surface fluxes at the measurement sites as a result of atmospheric transport only. This matrix is efficiently computed using the adjoint version of our CTM since the number of measurement stations is small compared with the number of surface flux parameters [Kaminski *et al.*, 1999a]. Since the atmospheric transport acts linearly on the concentration and the sources are assumed to be independent of the atmospheric methane mixing ratio, the corresponding terms in (4) are linear.

The matrix  $\mathbf{S}$ , representing the concentration response to methane sinks in the atmosphere, is calculated using the standard “forward” model version. First, the tropospheric OH distribution is computed using the full chemistry version [Houweling *et al.*, 1998]. The OH fields obtained are used in a methyl chloroform ( $\text{CH}_3\text{CCl}_3$ ) simulation and scaled to give an optimal fit to observed  $\text{CH}_3\text{CCl}_3$  concentrations (see section 6). In a second model run these scaled OH fields are used to compute the  $\frac{\partial Q_{k,l}}{\partial s_{OH}}$  using  $[\tilde{\text{CH}}_4]$ . The stratospheric sink response is determined in a separate run of the forward model using the prescribed sink distribution.

A model spin-up time of 3 years has been applied to derive both matrices in (4), with the responses being stored in the fourth year. In each year of model simulation the same sources and sinks are used. According to Hein *et al.* [1997] and Tans [1997] a period of 3 years is sufficiently long for the atmosphere to be well mixed. As a result, the global-scale concentration gradients, caused by the constant fluxes, change little after this period, and the initial concentrations contribute to the global mean only.

The solution to the inverse flux optimization is defined as the set of parameter values that optimally satisfy two requirements. First, the optimized or a posteriori fluxes should be as close as possible to the first-guess (a priori) fluxes. Second, the inversion-derived (a posteriori) fluxes should lead to an as close as possible agreement between modeled and measured concentrations. In both instances, misfits are quantified as sums of squares in units of observational and a priori standard deviations, respectively. Mathematically, this solution

corresponds to the minimum of a cost function  $\mathcal{J}$  defined as

$$\mathcal{J}(x) = \langle \mathbf{d}(x) - \mathbf{d}_{obs}, \mathbf{C}_d^{-1}(\mathbf{d}(x) - \mathbf{d}_{obs}) \rangle + \langle \mathbf{x} - \mathbf{x}_{apr}, \mathbf{C}_{x,apr}^{-1}(\mathbf{x} - \mathbf{x}_{apr}) \rangle, \quad (5)$$

where  $\langle \rangle$  denotes an inner product, the subscripts *obs* and *apr* denote observed and a priori values, and  $\mathbf{C}_d$  and  $\mathbf{C}_{x,apr}$  are the covariance matrices for the corresponding vectors  $\mathbf{d}_{obs}$  and  $\mathbf{x}_{apr}$  ( $\mathbf{x}$  contains both  $\mathbf{f}$  and  $\mathbf{s}$ ). It can be shown that at the minimum of  $\mathcal{J}$  the fluxes satisfy

$$\mathbf{x} = \mathbf{x}_{apr} + (\mathbf{A}^T \mathbf{C}_d^{-1} \mathbf{A} + \mathbf{C}_{x,apr}^{-1})^{-1} \mathbf{A}^T \mathbf{C}_d^{-1} (\mathbf{d}_{obs} - \mathbf{A} \mathbf{x}_{apr}), \quad (6)$$

where matrix  $\mathbf{A}$  contains both  $\mathbf{T}$  and  $\mathbf{S}$  [Tarantola, 1987]. A second, equally important, result of the inversion is the uncertainty of the inferred parameters, which is derived from the uncertainties of the observations and the uncertainties of the a priori estimates. The a posteriori covariance matrix of the uncertainty in the inferred parameters is [Tarantola, 1987]:

$$\mathbf{C}_x = (\mathbf{A}^T \mathbf{C}_d^{-1} \mathbf{A} + \mathbf{C}_{x,apr}^{-1})^{-1}. \quad (7)$$

Technically, (6) and (7) are solved by means of a singular vector decomposition.

### 3. Model Description

In this study we use the “off-line” global 3-D atmospheric Transport Model 2 (TM2) developed by Heimann [1995]. The spatial resolution of the model is  $10^\circ$  in the longitudinal direction and  $7.8^\circ$  in the latitudinal direction with nine vertical sigma levels from the surface up to 10 hPa ( $\sim 30$  km altitude). The horizontal and vertical transport of tracers is based on 12 hourly mean air mass fluxes and sub-grid scale transport data. For this purpose, analyzed meteorological fields from the European Centre for Medium-Range Weather Forecast (ECMWF) model have been preprocessed as described by Heimann and Keeling [1989] and Heimann [1995]. In the present study, ECMWF-analyzed data for the year 1987 have been used for each year of model simulation.

The advective transport is calculated using the “slopes scheme” of *Russell and Lerner* [1981]. The sub-grid scale convective mass fluxes are evaluated using the cloud scheme of *Tiedke* [1989], which includes entrainment and detrainment in updrafts. Turbulent vertical transport is based on stability-dependent vertical diffusion [*Louis*, 1979]. The tracer transport has been validated by comparing  $^{85}\text{Kr}$ ,  $\text{SF}_6$ ,  $^{222}\text{Rn}$ , and CFC-11 measurements to simulations. The results indicate that the boundary layer mixing over the continents is reasonably well represented. The cross-equatorial transport, however, is somewhat underestimated in the model (see section 6).

To compute relationships between fluxes and concentrations efficiently, an adjoint version of the model has been used. The adjoint model was developed by *Kaminski et al.* [1996] using the tangent-linear and adjoint model compiler (TAMC) by *Giering* [1996]. This model has previously been applied in a study of the global sources and sinks distribution of  $\text{CO}_2$  [*Kaminski et al.*, 1999b].

To simulate the interactions between methane and tropospheric photochemistry, the forward code has been extended with the photochemistry routine of *Houweling et al.* [1998]. Chemical equations are integrated using a Eulerian backward iterative (EBI) scheme as formulated by *Hertel et al.* [1993]. Emissions of photochemical tracers other than  $\text{CH}_4$  are based on Global Emission Inventory Activity (GEIA) and Emission Database for Global Atmospheric Research (EDGARV2.0) inventories [*Olivier et al.*, 1996; *Guenther et al.*, 1995; *Yienger and Levy*, 1995; *Benkovitz et al.*, 1996]. The treatment of wet and dry deposition of tracers is comparable to *Houweling et al.* [1998]. Photolysis rates are derived from the radiation code of *Brühl and Crutzen* [1988], and daytime average values are updated twice a month. As a first-order approximation of the diurnal variation of photolysis rates, a single period of a normalized  $(\sin)^2$  function is used during daytime.

## 4. Measurements

Observational data have been derived from measurements at 34 monitoring stations and 11 positions along two cruise tracks of the National Oceanic and Atmospheric Administration (NOAA)/ Climate Monitoring and Diagnostics Laboratory (CMDL) cooperative air sampling network [Dlugokencky *et al.*, 1994b] (see Table 1). In general, a duplicate sample at each station is taken about once a week. The precision of the gas chromatographic analysis is estimated at 0.2% [Dlugokencky *et al.*, 1994b]. Measurements “flagged” by NOAA, indicating that the sampled air may have been influenced by local sources, have not been used.

**Table 1.**

The NOAA methane concentration records show significant interannual variability caused by year to year differences in methane fluxes and atmospheric circulations. These variabilities cannot be reproduced by the model since the same fluxes and winds are used for each year of model simulation. The assumption of constant fluxes implies that a constant methane trend is also computed. To satisfy this assumption as much as possible for recent years, we have chosen January 1993 until December 1995 as a target period. Stations with a regular data record over this period have been selected. At each station a multiyear averaged seasonal cycle and a spline fit to the trend have been computed, on the basis of data sampled over this target period.

A global mean surface CH<sub>4</sub> trend has been derived from a linear fit to the spline trends at 21 selected background locations (see Table 1). For this purpose, stations were selected from which a reliable trend over this relatively short target period could be derived, favoring remote stations with little data gaps. In this way we computed a trend of 6.1 ppbv yr<sup>-1</sup> with a 1σ uncertainty interval of 1.2 ppbv yr<sup>-1</sup> over the period 1993–1995. For the 5.06x10<sup>18</sup> kg atmospheric load in our model this corresponds to 17.1 ± 3.5 Tg(CH<sub>4</sub>) yr<sup>-1</sup>. From the global mean trend  $\mathcal{T}$ , the multi-year averaged seasonal cycle  $\mathcal{S}$ , and the intercept  $I$  per station at the midpoint of the target period ( $t_{mid}$ ) the observations are derived as

$$d_{obs}(i, t) = I_i + (t - t_{mid})\mathcal{T} + \mathcal{S}_{i,t}. \quad (8)$$

The uncertainty in the derived monthly mean concentration is taken to be the root mean square of the residual between the averaged duplicate samples and the fitted data as derived from (8). The contribution of the analysis error to the uncertainty is small and has therefore been neglected. This data-fitting procedure is described in detail by *Hein et al.* [1997].

The ship-based measurements over the Pacific (P01–P05) and South China Sea (SC1–SC7) have been sampled at  $5^\circ$  and  $3^\circ$  latitude intervals, respectively. Because of variations in the cruise tracks, the longitudinal coordinates of the cruise measurements are not constant. From the cruise-specific coordinates (E. J. Dlugokencky, personal communication, 1997) average longitudes have been computed. Data from cruises that followed alternative tracks have been rejected. Variations in the longitudinal coordinates are generally within  $10^\circ$  over the Pacific and  $2^\circ$  over the South China Sea. These differences are considered to be reasonably small given the horizontal resolution of our model and the relatively smooth methane concentration gradients over the Pacific. The Pacific locations P01–P05 are only a minor subset of all Pacific cruise locations at which samples are taken by NOAA. For the remaining locations, however, too little data were available over the target period to derive reliable seasonal cycles.

## 5. A Priori Assumptions

Recent estimates of the global distribution and annual total for each surface source and sink process have been used as a priori inputs. Table 2 lists all the surface fluxes accounted for, the associated annual totals, and the assumed uncertainties per process. It should be noted that the applied inverse modeling formalism (as outlined in section 2) requires that the first-guess information be independent of the measurements. The applied emission distributions to a large degree satisfy this requirement, being merely based on bottom-up derived statistics of, for example, population density, industrially produced quantities, etc. The global budget may well have been taken into consideration, however, in establishing the first-guess annual total and corresponding uncertainties. Although, formally, it is incorrect to use these numbers, they

are being used in this study for lack of alternative estimates. In this section, only those sources and sinks are discussed that are not fully explained by the references listed in Table 2. Section 6 discusses the a priori treatment of the tropospheric sink. **Table 2.**

On the basis of a compilation of methane measurements in seawater [*Lambert and Schmidt, 1993*], methane fluxes from open oceans and coastal zones have been estimated as 3.6 and 6.1 Tg(CH<sub>4</sub>) yr<sup>-1</sup> respectively. In addition, about 5 Tg(CH<sub>4</sub>) yr<sup>-1</sup> of methane is assumed to be emitted from seepages through the sediments of continental shelves. Open ocean and continental shelf emissions are assumed to be uniformly distributed, where the continental shelves have been defined as the coastal zone with sea depths <200 m.

The global distribution of methane emissions from wild ruminants have been approximated using the method described by *Bouwman et al. [1997]*. As proposed by *Warneck [1988]* 3–6% of the net primary produced (NPP) vegetation is consumed by wild animals of which a constant fraction is assumed to be emitted as methane. We used an annual NPP distribution as derived from the Integrated Model to Assess the Greenhouse Effect (IMAGE) [*van Minnen et al., 1996; Kreileman, 1996*] discarding cultivated regions on the basis of land use database by *Matthews [1983]*. Similar to *Bouwman et al. [1997]*, we assume that in forested ecosystems only 20% of NPP consists of consumable grass or leaves. Vegetation types have been assigned on the basis of the landcover database by *Olson et al. [1983]*.

Sulphur emissions are used as a proxy for methane emissions from volcanic degassing using the time-averaged distribution of volcanic sulphur emissions from continuously emitting volcanoes on the basis of *Andres and Kasgnoc [1998]* scaled to 3.5 Tg(CH<sub>4</sub>) yr<sup>-1</sup> [*Lacroix, 1993*]. Biomass burning emission estimates by *Hao et al. [1991]* and *Olivier et al. [1996]* do not account for the contribution by the Australian continent. In this study these emissions have been derived from estimated forest and savanna burning over Australia (L. Bouwman, personal communication, 1998). We compute that the Australian biomass burning source contributes 6% to the global total, assuming the same methane release per unit biomass for each continent. The seasonal cycles of Australian biomass burning emissions have been estimated using

monthly averaged precipitation based on 5 years of ECMWF output (1992–1996). The length and the distribution of the emissions over the burning season are taken from *Hao et al.* [1991], with the start of burning season in the second month of the dry period.

Uncertainty estimates of methane sources and sinks are mainly available for the globally and annually integrated fluxes. Since the a priori uncertainties per grid cell are needed we scale these integrated values down to “local” uncertainties  $\sigma_{i,j}$  for the flux by process  $i$  in each surface grid cell and month (index  $j$  for both) in which the process is active. Subsequently, for each surface grid cell we compute the combined uncertainty of the flux due to all active processes. It has been assumed for each process  $i$  that (1) the relative uncertainties  $k_i$  of emissions  $f_{i,j}$  from each active grid cell in each month are constant ( $\sigma_{i,j} = k_i f_{i,j}$ ) and that (2) the local uncertainties  $\sigma_{i,j}$  are uncorrelated ( $\sigma_i^2 = \sum_j \sigma_{i,j}^2$ ). Assuming that in a particular grid cell and month the local uncertainty of the fluxes due to all active processes are independent, the local uncertainties for the sum of these fluxes  $\sigma_j$  are given by:

$$\sigma_j = \sqrt{\sum_i (k_i f_{i,j})^2}. \quad (9)$$

As a consequence, the local relative uncertainties are much larger than uncertainties in the globally integrated emissions (see also section 7). This procedure for our standard inversion is modified in testing the effect of spatial and temporal correlations in section 8.

## 6. Chemical Methane Loss

About 90% of the methane removal from the atmosphere is due to reaction with the hydroxyl radical in the troposphere. This means that to simulate the methane cycle accurately, a realistic representation of OH is of critical importance. Methyl Chloroform (1,1,1 trichloroethane, called  $\text{CH}_3\text{CCl}_3$  hereafter) can be used to constrain OH, because its sources are relatively accurately known, and the hydroxyl radical reaction constitutes the most important sink. To test and optimize the model-simulated hydroxyl radical fields, a simulation of  $\text{CH}_3\text{CCl}_3$  has been carried out. Simulated  $\text{CH}_3\text{CCl}_3$  concentrations have been

compared to measurements from five stations of the Atmospheric Lifetime Experiment (ALE)/Global Atmospheric Gases Experiment (GAGE) network from 1978 to 1994 [Prinn *et al.*, 1992, 1994].

To simulate  $\text{CH}_3\text{CCl}_3$ , surface emissions are applied on the basis of Midgley [1989] and Midgley and McCulloch [1995]. Ocean uptake and stratospheric and tropospheric loss have been represented according to Kanakidou *et al.* [1995]. The calculated turnover time of  $\text{CH}_3\text{CCl}_3$  due to ocean uptake amounts to 92 years, well within the range of 59–128 years estimated by Butler *et al.* [1991]. The stratospheric turnover time has been scaled to  $\sim 50$  years, in agreement with Kanakidou *et al.* [1995]. A scaling factor  $\alpha_{OH}$  for the global OH field has been computed minimizing the r m s differences between measured and simulated  $\text{CH}_3\text{CCl}_3$ , weighted by the reciprocal standard deviations of the monthly mean measurements, similar to Hein *et al.* [1997]. These weighting factors also take into account a 5% systematic uncertainty in the absolute calibration of the  $\text{CH}_3\text{CCl}_3$  measurements [Prinn *et al.*, 1995]. The minimum is evaluated using the method of Brent [1973], applying inverse parabolic interpolation. This procedure yields an optimized scaling factor  $\alpha_{OH} = 0.95$ , which has subsequently been used to scale the OH fields. The corresponding atmospheric lifetime of  $\text{CH}_3\text{CCl}_3$  amounts to 5.0 years, which is on the high end of the range of  $4.8 \pm 0.3$  years calculated by Prinn *et al.* [1995]. Krol *et al.* [1998] derived an even lower lifetime of 4.5–4.7 years over the period 1978–1993, taking into account a possible trend in the hydroxyl radical concentration. The optimized hydroxyl radical level leads to a troposphere-integrated methane turnover time of 9.0 years. This corresponds to the oxidation of 485 Tg of methane per year for a concentration level representative of 1994. The uncertainty in the tropospheric OH content is estimated at  $\sim 10\%$  by Krol *et al.* [1998]. We apply a  $2\sigma$  uncertainty, which is a factor of 2 smaller than this estimate (25 Tg( $\text{CH}_4$ );  $\sim 5\%$ ), to keep the a posteriori derived sink within a reasonable range (see section 10).

Figure 1 shows a comparison between simulated and measured  $\text{CH}_3\text{CCl}_3$  concentrations at the 5 sites of the ALE/GAGE network. From Figure 1 it appears that the latitudinal gradient

**Figure 1.**

of  $\text{CH}_3\text{CCl}_3$  is overestimated by the model. This indicates that tracer transport in the model is too slow and/or that the simulated ratio between the Northern and Southern Hemispheric (NH/SH) OH content is too low. Indeed, on the basis of  $^{85}\text{Kr}$ ,  $\text{SF}_6$ , and CFC-11 simulations we conclude that the interhemispheric exchange time is underestimated by  $\sim 20\%$ , in line with earlier findings [Hein, 1994; Heimann and Keeling, 1989]. From simulations carried out with the horizontal and vertical diffusion coefficients tuned to reproduce these tracers optimally, we conclude that transport explains about half of the underestimation of the  $\text{CH}_3\text{CCl}_3$  gradient. We aim to improve this as part of future model developments.

## 7. Methane Inversion Results

Figures 2 and 3 show comparisons of first-guess and optimized surface fluxes of methane.

The per grid differences appear to be significant, with values of the same order as the assumed first-guess fluxes. As a result, flux parameters that are a priori assigned to be net sources of methane may represent a net sink a posteriori and vice versa. The changes are mainly limited to the continents, which is explained by the relatively small a priori uncertainty in the oceanic flux. Over the continents, regions with relatively strong emission increases are typically adjacent to regions with strong decreases, for example, over southeast Asia during summer. Clearly, the simulated concentrations are most sensitive to flux changes in those grid boxes, in which measurement sites are located. Consequently, in these grid boxes relatively small flux adjustments can compensate for misfits between simulated and modeled concentrations. This is also illustrated by maps of this sensitivity for  $\text{CO}_2$  as given by Kaminski *et al.* [1999b]. To satisfy large-scale budget constraints, these corrections are then compensated for elsewhere.

Concentrations as computed using a priori and a posteriori flux fields have been compared to observations (Figure 4). As expected, the optimized flux field improves the agreement between modeled and measured concentrations. In general, the a priori flux field appears to overestimate the global north–south methane concentration gradient significantly. Figure 5

**Figure 2.**

**Figure 3.**

**Figure 4.**

shows that this feature, particularly, has been corrected in the optimization. A decrease of the latitudinal concentration gradient can be achieved in two different ways: first, by a decrease in the ratio between the emissions in the Northern and Southern Hemispheres and, second, by a decrease of the globally integrated sources and sinks. The latter will not affect the globally integrated methane burden provided that the difference between the integrated sources and sinks matches the trend in methane. In fact, many combinations of sources and sinks satisfy this global budget constraint. It can be verified, however, that the latitudinal concentration gradient is related to this combination such that larger sources and sinks lead to an increased gradient. From the differences in the a priori and a posteriori integrated flux totals (Table 3) it appears that both mechanisms contribute to the decreased a posteriori latitudinal gradient.

**Figure 5.**

**Table 3.**

Regional-scale flux changes can often be explained by examining the fits at the nearest stations. For example, the decreased emissions over central China in Figure 3 are largely imposed by the South China Sea cruise measurements. In autumn, when predominantly continental air is sampled at these sites, measured concentrations are significantly lower than predicted by a model simulation using a priori flux fields. Therefore a better fit at these sites is obtained when fluxes over central China are reduced. Indeed, excluding the South China Sea cruises from the inverse optimization almost completely eliminates the region of decreased emissions over China in Figure 3. Also, measurements at the Mongolian station Ulaan Uul and Qinghai Province in central China support a decrease in methane emissions over central China relative to the a priori assumptions. The simulated concentrations at these higher-altitude stations are, however, less sensitive to emission adjustments in this region and therefore impose weaker constraints.

A decrease in the a posteriori estimated emissions over southeast Australia is a persistent feature over all seasons. This is related to the measurements at Cape Grim and is most probably caused by the fact that these measurements and the model simulated concentrations at this station represent something different. At Cape Grim air is sampled only if the wind direction is between west and southwest to avoid contamination by local sources. As a result

of this baseline selection, monthly mean measurements are expected to be lower than those calculated by the model since in the model such a sampling protocol is not used. As shown by *Ramonet and Monfray* [1996] for CO<sub>2</sub>, the seasonal cycle at this station is also influenced by the sampling procedure.

The emission decrease over Europe, extending over northwest Russia, appears not to be imposed by the measurements of the European stations at the Baltic Sea, Mace Head, Gozo, and Ocean Station M. Removing these stations from the inverse optimization only slightly influences the a posteriori emission patterns over these regions. Since the a posteriori tropospheric OH sink has decreased as compared with the first guess, decreased fluxes help balance the concentration level. In other words, the a posteriori flux reductions in these regions are more strongly imposed by the global budget than by the regional observations.

The South American continent is poorly sampled by the observational network. Ascension Island, which is at a relatively small distance from South America, predominantly samples air transported from the African continent [*Kaminski et al.*, 1999b]. Other stations are at large distances where plumes of continental air have largely been dispersed. As a result, the flux changes relative to the a priori assumptions over South America are not caused by particular misfits at a few stations but rather contribute to the average level and seasonal cycles at a large number of stations. Since most of these stations are surrounded by oceanic grid boxes, which are all part of a larger flux region, local flux adjustments are suppressed. Flux adjustments at the continents need to be larger to compensate for the lower sensitivities at the oceanic stations. The standard deviations of the measurements at remote Southern Hemispheric stations like the South Pole, Palmer Station, and Syowa are, however, relatively small, and therefore these measurements receive a relatively large weight in the inversion. Therefore, despite their relatively low sensitivity these measurements can still constrain the estimated continental source strengths.

Figure 6 shows the reduction in the surface flux uncertainty as a result of flux constraints imposed by observational data in the inversion. Evidently, the uncertainty reduction is most

**Figure 6.**

pronounced in the direct vicinity of continental measurement stations. From (7) it follows that the uncertainty reduction is determined by two factors: (1) the a priori uncertainty relative to the measurement uncertainty and (2) the sensitivity of the simulated concentration at a station toward the fluxes. If both factors are relatively large, as is the case for these continental fluxes, the uncertainty reduction is relatively strong as well. At some locations a significant uncertainty reduction is computed at larger distance from the measurement sites. For example, the spot with relatively strong uncertainty reduction in Angola (Figure 6) is related to constraints from the measurements at Ascension Island. At oceanic stations, no sharp sensitivity maxima are found because of to the aggregation of oceanic fluxes. Since, in addition, the a priori uncertainties assigned to the oceanic emissions are relatively low, the computed uncertainty reduction over the ocean is low.

The difference in the integrated uncertainties in Table 3 and the uncertainty reduction per grid in Figure 6 indicates that the relative uncertainty reduction increases toward larger scales. Such strong uncertainty reductions can only be explained if the a posteriori uncertainties in the contributing grids are predominantly anticorrelated. Figure 7 shows the covariances of the a posteriori uncertainties of all surface fluxes for July and two flux elements in central China and in Brazil. Indeed, the uncertainties in the a posteriori fluxes are predominantly anticorrelated with respect to the single elements. Such anticorrelations indicate that the grid box fluxes are not resolved by the measurements. In other words, the sum of a cluster of parameters is constrained by the measurements rather than by the contributions of individual elements. The covariance plot for the Chinese flux element shows a dipole structure similar to the flux differences in Figure 2. This confirms that such structures are imposed by regional budget constraints.

The validation of the a posteriori flux fields is difficult since it would require a source of information independent of those already used in the inversion. Alternatively, we can perform a series of inversions in each of which we omit the information of one of the stations. Such a test shows to what extent the inversion-derived emission fields improve the simulated

**Figure 7.**

methane concentrations. Figure 8 shows results of these tests at different sites. In particular, at the remote stations over the oceans (GMI and ASC) the agreement between simulated and measured concentrations has improved. At continental sites, such as Grifton, North Carolina (ITN), concentrations are determined by the source and sink composition in the direct surroundings of a station. Therefore the agreement is expected to be worse there. As illustrated in previous studies [*Kaminski et al.*, 1999b; *Plumb and Zheng*, 1996], the singular vectors can be used to determine in which direction in the flux space the measurement information is most efficiently mapped. Although these studies focus on different trace gases (CO<sub>2</sub> and CFCs, respectively), similar features are found for methane. Such an analysis indicates that a few directions are relatively well resolved, i.e., the global mean mixing ratio, the latitudinal gradient, and the seasonal cycle. From Figure 8 it can be seen that indeed, the main improvements in the a posteriori flux derived concentrations are related to these features.

**Figure 8.**

To quantify the amount of information in the observations of particular stations, inversions have been carried out in which only a single station is used. Table 4 shows a ranking of stations according to their globally and locally integrated uncertainty reduction. Here local has been defined as the grid box in which a station is located plus all grid boxes adjacent to this grid box (nine in total), which means all emissions within a range of ~1500 km. The uncertainty reduction has been divided by the uncertainty reduction in a full (45 station) inversion. In other words, this uncertainty reduction represents the percentage of uncertainty reduction in a full inversion, which can already be achieved by introducing only a single station.

From the size of the globally integrated uncertainty reductions in Table 4 it is clear that in a multistation inversion the uncertainty reduction per station is less than in the single station inversion. The reason for this follows directly from (7). On the global scale, remote stations as, such as SPO and SYO, have the largest impact on the uncertainties. This can partly be explained by the relatively small uncertainties of these measurement data owing to the relatively small variability at these stations. Furthermore, the uncertainty in the local fluxes

**Table 4.**

is relatively small so that fluxes at a greater distance receive relatively more weight. Lowest in rank on the global scale are stations for which the opposite argument holds. Generally, stations with a high score in reducing global-scale uncertainties have a low score on the local scale and vice versa. This analysis is dependent on the a priori assigned uncertainties and the Jacobian matrix  $A$ . Therefore the exact order may be quite different when using other a priori uncertainties or when studying a different trace gas.

## 8. Sensitivity Tests

In the previous section it was assumed that all errors in the measurements and fluxes are uncorrelated. One can think, however, of realistic conditions that violate this assumption. In fact, correlations may even serve as additional constraints on the fluxes. Consider, for example, the European continent, with the most prominent methane sources being intensive farming and industrial processes. None of these sources are expected to change substantially over the seasons. Hence it is likely that these sources and related errors are positively correlated in time. Another example is the use of emission factors that are, for instance, derived from statistics of fossil fuel use or food production. A bias in such emission factors may lead to correlated errors both in space and time. Emission factors are often relatively uncertain since they are generally based on only a few case studies, which have been extrapolated to large regions. Provided that it is reasonable to assume that emission factors are constant, such biases may indeed occur. It can be argued, however, that the largest uncertainty introduced by using emission factors is in the assumption that they are constant. At smaller distances between sources, however, the assumption of constant emission factors is probably less violated since source processes are expected to be more similar. In this case the correlation is expected to increase with decreasing distance.

Regarding the measurements, for instance, systematic errors in the sampling analysis lead to positively correlated errors. For the NOAA glass flask analyses, however, such errors are expected to be small since the same calibration standard is used for all stations. Probably,

the representativity of point samples for the time- and spaceaveraged concentrations computed by the model is a much larger source of errors. Although the measurements are screened for “pollution events,” the remaining samples may still be influenced by conditions that the model is not able to reproduce. Only in some special cases may such representation errors may also be correlated. For example, systematic differences in the origin of air masses sampled in the model and measurements, as is the case, for example, at Cape Grim, introduce positively correlated errors. In general, however, representation errors are expected to be dominated by random influences of “coincidental” events. Therefore it seems reasonable to assume that measurement errors are uncorrelated.

The information needed to quantify spatial and temporal correlations in the fluxes is practically absent. In general, uncertainty analyses of emission inventories are scarce, and if present, they come in a wide range of different forms that cannot readily be combined for purposes such as the present study. To investigate the importance of a priori assumed correlations, two sensitivity tests have been carried out, one for temporal and one for spatial correlations.

Figure 9 shows estimated seasonal cycles of the fluxes in some selected grid boxes. In the time-correlated inversions a correlation coefficient of 0.9 has been applied to monthly averaged surface fluxes at the same location representing different months. In addition, for sources that are known to be strongly dependent on the season, for example, biomass burning, rice cultivation, and natural wetlands, a temporal correlation length of 2 months has been taken into account. In these cases the correlation is assumed to decrease exponentially in time. The correlation length is defined as the time in which the correlation decreases by a factor  $1/e$ . Such time dependent correlations lead to a smoothing of the estimated seasonal cycles. The timing and length of the season, which are generally quite uncertain for these sources, can still be adjusted by the measurements.

Both for the Pacific Ocean and central Europe (see Figure 9) the a posteriori seasonal cycles are influenced substantially by the assumed time correlation. Assuming uncorrelated

**Figure 9.**

sources, the computed seasonal variations cannot be explained by the most probable processes involved. The time-correlated seasonal cycles are considerably closer to their first guesses. Also, at the Chinese and African sites the time-correlated cycles are substantially closer to the first guess, despite the larger freedom for flux adjustments, because of to the 2 month correlation length assigned to biomass burning and rice paddy emissions. In Zambia the biomass burning peak during the dry season is suppressed in the time-correlated inversion. Since biomass burning emissions may well peak in one particular month, the smoothing of the emissions in the time correlated inversion probably does not improve the results for this location.

In Figure 10, differences between first-guess and optimized fluxes are presented using spatial correlations. A spatial correlation coefficient of 1.0 with a correlation length of 2000 km ( $\sim 3$  grid cells) has been applied to all sources. Probably, for some sources the spatial distribution is better known than for others, which is, for example, the case for ruminants compared with biomass burning. This would justify the use of source-specific correlations. Since we lack the information to quantify these differences, all processes are treated the same. Note that inversions that differ in the assumed correlations also have different local a priori flux uncertainties since additional correlation terms appear in equation (9). Since no anticorrelations are used and the same global uncertainties are assumed, the local uncertainties will, as a result, become smaller. As a consequence, the a priori information on the fluxes receive more weight. A comparison of Figures 10 and 2 indicates that spatial correlations significantly change the estimated fluxes. As expected, emission changes extend over larger regions. Compared with the time-correlated inversion, it is difficult to determine whether or not the use of space correlations improves the results. Little is learned from a comparison as presented in Figure 8 since the differences between the concentrations derived from the correlated and uncorrelated inversions appear to be small.

Two additional sensitivity tests have been carried out to test the influence of the assigned a priori uncertainties (also listed in Table 5) that determine the weights of misfits in the

**Figure 10.**

cost function. One may question how fair this weighting is since these uncertainties are, in general, poorly quantified. The method to derive grid-scale uncertainties from global-scale estimates has been selected for its mathematical consistency but, in fact, does not give very realistic values. The assumed global uncertainty estimates, as listed in Table 2, lead to relative uncertainties per source per grid per month of  $\sim 600\%$ . Since Gaussian probability distributions are assumed that do not conserve sign, grids a priori dominated by sources could a posteriori easily be changed into sinks. In regions where a change in sign of the a priori assumed flux is unrealistic it is not appropriate to assume a Gaussian distribution. To investigate the sensitivity of estimated emissions to a priori prescribed flux uncertainties, two sensitivity simulations have been carried out. In the first simulation it is assumed that we do not know whether one source is more uncertain than another. Therefore each surface flux is assigned the same relative uncertainty, taken to be  $600\%$ , except for the oceans. In the second inversion, similar to the first, every surface flux is considered to be equally well (or poorly) known; an uncertainty level of  $100\%$  is chosen so that changes in signs are always outside the  $1\sigma$  interval.

Finally, an inversion is performed in which the ratio in the OH radical abundance of the Northern and Southern Hemispheres has been changed. A ratio of 2 (NH/SH) has been chosen, which, using a priori fluxes only, leads to a simulated latitudinal methane concentration that is almost correct. The OH field, as derived from the tropospheric chemistry version of our model, has a NH/SH ratio of 1.06. Thus, in this sensitivity test the overestimated methane gradient is compensated by adjusting the OH distribution.

To quantify and illustrate the results of sensitivity tests, fluxes have been integrated over hemispheres and regions. Obviously, the sensitivity of the optimized fluxes to a certain assumption is dependent on the weight the tested assumptions receive in the inversion. Since only a priori assumptions are tested, these weights are approximately determined by the relative weights of a priori and measurement constraints. Therefore two regions have been defined: region 1 over southeast Asia ( $75^{\circ}$ – $135^{\circ}$ E,  $10^{\circ}$ – $40^{\circ}$ N), which is relatively well

resolved by the measurements and Region 2 over central Africa (5°W–35°E, 15°S–25°N), which is relatively poorly resolved by the measurements. Table 5 summarizes these integrated emissions and the associated uncertainties for all sensitivity tests performed.

**Table 5.**

Overall, the a posteriori estimates are rather similar compared with the differences between a priori and a posteriori estimates. Even for the African region, which is relatively poorly sampled, the estimated totals are quite robust. The a priori and a posteriori uncertainties are so high, however, that none of the differences in Table 3 are significant. Looking at the global totals, surprisingly, the spatially correlated and 100% relative uncertainty inversions, which both have relatively low a priori uncertainties compared to the standard simulation, have the highest adjustments in the globally integrated fluxes. The Northern versus Southern hemispheric emission ratio, however, is closer to the a priori value. A different compromise between globally integrated flux adjustment and north–south emission adjustment to correct for the simulated latitudinal concentration gradient is favored in these inversions. The inversion in which the OH ratio has been adjusted shows that both the north–south emission ratio and the globally integrated source and sink are close to their a priori values, which is again explained by the corresponding effects on the latitudinal gradient in methane.

## 9. Case Study: Emissions From Southeast Asia

Rice agriculture constitutes an important methane source in southeast Asia. Its relatively high uncertainty results from the high temporal and spatial variability in the source strength of rice paddies and the relatively poor statistics on rice management in developing countries. Recent studies [*Huang et al.*, 1997; *Denier van der Gon*, 1998] point to a global source strength in the lower part of the range of the IPCC estimate of  $60 \pm 40 \text{ Tg}(\text{CH}_4) \text{ yr}^{-1}$  IPCC [1994] and of the  $80 \pm 50 \text{ Tg}(\text{CH}_4) \text{ yr}^{-1}$  [*Lelieveld et al.*, 1998] used in this study. On the basis of these recent studies and several estimates of the rice agriculture-related methane emissions in China [*Kern et al.*, 1995; *Cao et al.*, 1995; *Dong et al.*, 1996; *Yao et al.*, 1996; *Kern et al.*, 1997], H. A. C. Denier van der Gon (personal communication, 1998) derived a

best guess estimate of  $30 \pm 15 \text{ Tg}(\text{CH}_4) \text{ yr}^{-1}$ .

To test whether the inversion results are sensitive to the a priori emission scenario assumed, two inversions called "standard" and "low rice" have been compared in which each estimate has been used as a priori input. The low rice scenario equals the standard scenario except for a reduction in rice paddy emissions, for which tropical wetland emissions have been substituted. The global source estimates of these two processes are expected to be particularly influenced by global budget information; that is, neither are independent of the measurements. It is questionable, however, how well the measurements constrain the relative magnitudes of these sources. Table 6 lists the emissions derived from both inversions integrated over hemispheres, a zonal band ( $10^\circ$ – $40^\circ\text{N}$ ), and a region ( $75^\circ$ – $135^\circ\text{W}$  part of the zone). The *Matthews et al.* [1991] rice emission map indicates that  $\sim 80\%$  of the rice paddies are located in the selected zonal band, and  $\sim 75\%$  are confined to the region.

**Table 6.**

The a posteriori integrated emissions appear to be quite insensitive to the a priori scenario applied. Globally, both scenarios show decreased a posteriori totals compared with the first guesses. In the standard scenario the decrease over the region of intensive rice cultivation (31%) is relatively large compared with the Northern Hemispheric emission change (16%), which can be interpreted as a regional decrease superimposed on the global decrease. For the low rice scenario the opposite is found, with a regional decrease (8%) slightly smaller than the Northern Hemispheric emission decrease (11%). In summary, on the basis of the standard and low rice simulations, relatively low emissions over southeast Asia are defensible, however, not as low as those indicated above. On the basis of these results neither scenario can be ruled out. It should be emphasized that the methane optimization is dominated by global-scale changes in the emissions, which largely obscure regional-scale changes.

## 10. Discussion

Inverse modeling is a useful tool to complement bottom up estimates of global methane sources and sinks. An important question is to what extent inverse modeling can contribute.

Since many different procedures can be used to perform such an inversion, the answer may be different depending on the technique, the model, and the assumptions used. Since the measurement data set is limited, the use of a priori knowledge is necessary to constrain the inverse problem, i.e. to find the most likely emission scenario consistent with the measurements. Compared to previous methane studies [*Hein et al.*, 1997; *Brown*, 1993] that for computational reasons have to prescribe a few fixed flux patterns and optimize the corresponding scaling coefficients, we greatly release this rigid a priori constraint. In our case the system has a much higher degree of freedom to adjust fluxes. Because a priori knowledge is used as input, our inversion does not provide a fully independent emission estimate. Instead, a different type of result is obtained addressing three important topics. First, this technique helps to establish the consistency between estimated emissions and measured concentrations. Second, the most likely emission changes can be derived to reduce inconsistencies. Third, by combining constraints imposed by measurements and a priori knowledge, uncertainties are reduced.

Uncertainty reductions appear to be a function of scale, with larger reductions going to larger scales. This reflects a trade-off between resolution and uncertainty reduction, which is common in inverse problems. This means that at small scales the individual sources and sinks are not resolved by the measurements, except those close to measurement stations. Closer to the stations, however, the uncertainty reduction becomes increasingly affected by the resolution of the model. Generally, in inverse modeling, uncertainties are a measure of the range over which parameters may change given the constraints. This range is dependent on the dimension of the flux space. The higher the number of possible solutions, the more options there are to compensate for "outlying" fluxes while still keeping the constraints satisfied. Therefore, in general, modeled a posteriori uncertainties are expected to be underestimates of the real uncertainty since the real world is always more complex than the model. Indeed, compared to big region approaches, we find relatively high a posteriori uncertainties. Since in our inversion the resolution is less limiting, our uncertainty reductions are expected to be more

realistic.

The case study presented in section 9 illustrates the consequences this may have. The results of *Hein et al.* [1997] suggest that inverse modeling puts a strong enough constraint on rice paddy emissions to rule out one of the scenarios since the standard scenario is on the high side and the low rice scenario is significantly lower than their inverse modeling-derived 95% confidence interval for rice paddy emissions. In this study, however, both scenarios are still within this uncertainty range.

In addition to uncertainty estimates, a posteriori derived methane concentration distributions indicate how much we learn in the inversion. Such a comparison should be interpreted with care, however, since it is an indirect test of fluxes. It is a direct test of the methane concentration field, however, and as such, it leads to the conclusion that the a posteriori derived methane concentration distribution has improved. Obviously, this is useful for applications where methane concentration fields are needed rather than flux fields. Although the concentration field has improved, the flux field may give improved results for the wrong reason. As mentioned in section 7, this is the case when flux adjustments compensate for model errors.

In fact, all inconsistencies between measurements and modeled concentrations are attributed to the fluxes and the measurements since the model is assumed to be perfect. A useful diagnostic of model error is the interhemispheric exchange time. As discussed in section 6, simulation of  $^{85}\text{Kr}$ ,  $\text{SF}_6$ , and CFC-11 indicates that the exchange time is underestimated by  $\sim 20\%$ . As a test, the exchange rate was increased by horizontal diffusion [*Prather et al.*, 1987; *Keeling et al.*, 1989], which showed that transport explains at most half of the difference between the measured and the simulated methane gradient if the a priori values for the methane fluxes are used. As a consequence, the adjustments in the ratio between Southern and Northern Hemispheric emissions and globally integrated sources and sinks by the inversion, as shown in section 7, can partly be attributed to this model error. In addition, an error in the relative OH abundances of both hemispheres may also contribute.

Within the uncertainty ranges of the  $\text{CH}_3\text{CCl}_3$  test the OH ratio between both hemispheres may vary between about 0.5 and 2 (C. M. Spivakovsky, Three-dimensional climatological distribution of tropospheric OH: Update and evaluation, submitted to *Journal of Geophysical Research*, 1999). This indicates that the  $\text{CH}_3\text{CCl}_3$  test is not ideally suited for validating this ratio, at least for the period of  $\text{CH}_3\text{CCl}_3$  measurements that we used to test our OH fields. A north–south ratio of 2, in addition to a corrected interhemispheric exchange time in the model, can overcompensate the underestimated  $\text{CH}_4$  gradient. From an atmospheric chemistry point of view such a high interhemispheric OH ratio is highly unlikely and cannot be explained by the models. Quantification of such chemical constraints is, however, very difficult. Our results indicate that to estimate sources and sinks of methane on a global scale accurately a more accurate validation tool for the global OH radical distribution is needed.

The number of available measurements as compared with the number of unknowns continues to be an important limitation on inversion studies. Unless considerable progress in measuring methane from satellites is made, this is not expected to change much in the next decade. Alternatively, measurements of isotope ratios, which provide process-specific information, may be used. Studies by *Brown* [1995] and *Hein et al.* [1997], however, indicate that the isotopic data set available at present does not provide an important constraint. Here some progress may be expected in the future since more data will become available.

Alternatively, the source information contained in the measurements may be used more efficiently. For example, it is likely that by using multiyear averaged seasonal cycles, much information is lost. When, instead of using averaged data, the actual measured data are used, the methane inversion should be improved in a number of ways. Meteorological input representative of each year of the target period should then be used, as opposed to repeatedly using one year, as is done in this study. Furthermore, quantitative information about sources that have a high interannual variability, such as dependencies on precipitation and temperature, should be provided. Representation errors between measured and modeled concentration then become increasingly critical since coincidental disturbances are averaged out to a lesser

degree. These topics will be the focus of future work.

## 11. Conclusions

We presented an inverse modeling method to study the global-scale sources and sinks of methane. The measurements have been treated in accordance with the quasi-stationary state assumption, as by *Hein et al.* [1997], assuming a constant trend and a multiyear averaged seasonal cycle. The inversion has been performed at a relatively high spatial and temporal resolution (per grid and per month) over the continents using an adjoint version of the global transport model by *Kaminski et al.* [1999b]. Recent estimates of the sources and sinks of methane have been used as first-guess input, including minor sources such as oceans, volcanoes, termites, and wild animals.

The inversion-derived net global surface source of methane amounts to 505 Tg(CH<sub>4</sub>) yr<sup>-1</sup>, using a first guess of 528 Tg(CH<sub>4</sub>) yr<sup>-1</sup> for the target period 1993–1995. The relative contribution of the Northern Hemispheric sources decreases from 77 to 67%. The chemical sinks in the troposphere and stratosphere decrease from 485 to 451 Tg(CH<sub>4</sub>) yr<sup>-1</sup> and 40 to 37 Tg(CH<sub>4</sub>) yr<sup>-1</sup>, respectively. The computed a posteriori methane trend of 18 Tg(CH<sub>4</sub>) yr<sup>-1</sup> is well within the 17.1 ± 3.5 Tg(CH<sub>4</sub>) yr<sup>-1</sup> as derived from the measurements over the target period 1993–1995. Simulations of <sup>85</sup>Kr, CFC-11, and SF<sub>6</sub> indicate that our model underestimates the interhemispheric exchange rate by ~20%, which explains up to 50% of the differences between the a priori and a posteriori emission estimates. In addition, errors in the simulated north–south distribution of the hydroxyl radical may contribute to these differences. Within the ranges of uncertainty the combined effect of model errors could potentially explain the differences in the observed and simulated methane gradient, which underscores the importance of reliable tools to validate the interhemispheric transport rate and the hydroxyl radical distribution.

In addition to providing new "measurement"-consistent emission estimates, inverse modeling helps to reduce the uncertainties. These uncertainty reductions are strongly related

to scale. Small (<1%) reductions are computed at the grid scale, with some exceptions close to measurement stations. At the scale of hemispheres, uncertainty reductions as large as 75% are obtained, for example, from  $\pm 80$  a priori to  $\pm 20$  Tg(CH<sub>4</sub>) yr<sup>-1</sup> a posteriori for the Northern Hemisphere. The sharp uncertainty decrease with scale is reflected by the predominantly negative correlation of the a posteriori flux uncertainties, indicating that at the grid scale, fluxes are not resolved by the measurements.

The sensitivity of the inversion-derived emission estimates to a number of a priori assumptions, such as the assumed a priori uncertainties, the OH radical distribution, and uncertainty correlations, has been tested. The conditions used in each sensitivity test are within the ranges of uncertainty. Estimated emissions integrated over larger regions appear to be quite robust to these assumptions, except for the large-scale OH radical distribution, which could compensate for the emission adjustments derived using the standard scenario. Defining more accurately the a priori state in terms of spatial and temporal correlations among uncertainties helps to reduce the a posteriori uncertainties. Since the observational information for justifying the use of any strong positive or negative correlations in space is essentially lacking, the improvement is limited in this work. It may, however, be a useful constraint if more information were available. The use of temporal correlations leads to more significant improvements and helps, in particular, constrain seasonal cycles in the fluxes. We emphasize that source quantification by inverse modeling would benefit from bottom up estimates of source correlations, which could, for example, be derived from source process modeling.

As a case study, we have focused on emissions from rice fields in southeast Asia. The continental NOAA stations Qinghai Province, Tae-ahn Peninsula, and Ulaan Uul and the South China Sea cruises helped constrain the emission estimates for this region. The a posteriori derived fluxes point to lower emissions as compared to the a priori assumptions. A case study illustrates, however, that the uncertainty related to the a posteriori derived emissions is still too large to reduce the uncertainty of rice paddy emissions significantly. In fact, the present inversion method allows a larger range of fluxes from rice paddies than is reported by

*Hein et al.* [1997]. Since the use of a high-resolution inversion is expected to improve the uncertainty estimates, our larger uncertainty range is expected to be more realistic.

**Acknowledgments.** We thank E. J. Dlugokencky (NOAA) for providing all kinds of information about the NOAA sampling network and for the hospitality in letting us have a glimpse in the kitchen. Also, we are grateful to R. Hein (DLR) for a helpful introduction to inverse modeling and for kindly providing us data. Further, we would like to acknowledge a useful cooperation with H. A. C. Denier van der Gon (Department of Soil Science and Geology, Wageningen University). This work has been supported by the Dutch Global Change program, NOP project 951202.

## References

- Andres, R. J., and A. D. Kasgnoc, A time-averaged inventory of subaerial volcanic sulfur emissions, *J. Geophys. Res.*, *103*, 25,251–25,261, 1998.
- Bates, T. S., K. C. Kelly, J. E. Johnson, and R. H. Gammon, A reevaluation of the open ocean source of methane to the atmosphere, *J. Geophys. Res.*, *101*, 6953–6961, 1996.
- Benkovitz, C. M., M. T. Scholtz, J. Pacyna, L. Tarrason, J. Dignon, E. C. Voldener, P. A. Spiro, J. A. Logan, and T. E. Graedel, Global gridded inventories of anthropogenic emissions of sulfur and nitrogen, *J. Geophys. Res.*, *101*, 29,239–29,253, 1996.
- Bouwman, A. F., D. S. Lee, W. A. H. Asman, F. J. Dentener, K. W. van der Hoek, and J. G. J. Olivier, A global high-resolution emission inventory for ammonia, *Global Biogeochem. Cycles*, *11*, 561–587, 1997.
- Brent, R. P., *Algorithms for Minimization Without Derivatives*, chap. 5, Prentice-Hall, Englewood Cliffs, N. J., 1973.
- Brown, M., Deduction of fluxes of source gases using an objective inversion algorithm and a chemical transport model, *J. Geophys. Res.*, *98*, 12,639–12,660, 1993.
- Brown, M., The singular value decomposition method applied to the deduction of the emissions and the isotopic composition of atmospheric methane, *J. Geophys. Res.*, *100*, 11,425–11,446, 1995.
- Brühl, C., and P. J. Crutzen, Scenarios of possible change in tropospheric temperatures and ozone concentrations due to man's activities, estimated with a one dimensional coupled photochemical climate model, *Clim. Dyn.*, *2*, 173–202, 1988.
- Brühl, C., and P. J. Crutzen, MPIC two-dimensional model, *NASA Ref. Publ. 1292*, pp. 103–104, 1993.
- Butler, J. H., J. W. Elkins, T. M. Thompson, B. D. Hall, T. H. Swanson, and V. Koropalov, Oceanic consumption of CH<sub>3</sub>CCl<sub>3</sub>: Implications for tropospheric OH, *J. Geophys. Res.*, *96*, 22,347–22,355, 1991.
- Cao, M. K., J. B. Dent, and O. W. Heal, Methane emissions from China's paddyland, *Agr. Ecosyst. Environ.*, *55*, 129–137, 1995.

- Crutzen, P. J., The role of methane in atmospheric chemistry and climate, in *Ruminant Physiology: Digestion, Metabolism, Growth and Reproduction: Proceedings of the Eighth International Symposium on Ruminant Physiology*, edited by W. V. Engelhardt, S. Leonhardt-Marek, G. Breves, and D. Giesecke, pp. 291–315, Ferdinand Enke Verl., Stuttgart, Germany, 1995.
- Denier van der Gon, H. A. C., Changes in CH<sub>4</sub> emissions from rice fields from 1960 to the 1990s, 1, impacts of modern rice technology, *Global Biogeochem. Cycles*, 1998, in press.
- Dlugokencky, E. J., K. A. Masarie, P. M. Lang, P. P. Tans, and E. G. Nisbet, A dramatic decrease in the growth rate of atmospheric methane in the northern hemisphere during 1992, *Geophys. Res. Lett.*, 21, 45–48, 1994a.
- Dlugokencky, E. J., L. P. Steele, P. M. Lang, and K. A. Masarie, The growth rate and distribution of atmospheric methane, *J. Geophys. Res.*, 99, 17,021–17,043, 1994b.
- Dlugokencky, E. J., E. G. Dutton, P. C. Novelli, and K. A. Masarie, Changes in CH<sub>4</sub> and CO growth rates after the eruption of Mt. Pinatubo and their link with changes in tropical tropospheric UV flux, *Geophys. Res. Lett.*, 23, 2761–2764, 1996.
- Dlugokencky, E. J., K. A. Masarie, P. M. Lang, and P. P. Tans, Continuing decline in the growth rate of the atmospheric methane burden, *Nature*, 393, 447–450, 1998.
- Dong, H. M., L. Erda, Y. Li, M. J. Rao, and Q. C. Yang, An estimation of methane emissions from agricultural activities in China, *Ambio*, 25, 292–296, 1996.
- Enting, I. G., C. M. Trudinger, and R. J. Francey, A synthesis inversion of the concentration and  $\delta^{13}\text{C}$  of atmospheric CO<sub>2</sub>, *Tellus, Ser. B*, 47, 35–52, 1995.
- Fung, I., J. John, J. Lerner, E. Matthews, M. Prather, L. P. Steele, and P. J. Fraser, Three-dimensional model synthesis of the global methane cycle, *J. Geophys. Res.*, 96, 13,033–13,065, 1991.
- Giering, R., Tangent linear and adjoint model compiler, *Users Manual*, Max Planck Inst. for Meteorol., Hamburg, Germany, 1996.
- Guenther, A., et al., A global model of natural volatile organic compound emissions, *J. Geophys. Res.*, 100, 8873–8892, 1995.

- Hao, W. M., M. H. Liu, and P. J. Crutzen, Estimates of the annual and regional releases of CO<sub>2</sub> and other trace gases to the atmosphere from fires in the tropics based on the fao statistics for the period 1975-1980, in *Fire in the Tropical Biota*, edited by J. Goldammer, pp. 440–462, Springer, New York, 1991.
- Hartley, D., and R. Prinn, Feasability of determining surface emissions of trace gases using an inverse method in a three-dimensional chemical transport model, *J. Geophys. Res.*, *98*, 5183–5197, 1993.
- Heimann, M., The global atmospheric tracer model TM2, *Tech. Rep. 10 ISSN 0940-9327*, Dtsch. Klimarechenzentrum, Hamburg, Germany, 1995.
- Heimann, M., and C. D. Keeling, A three-dimensional model of atmospheric CO<sub>2</sub> transport based on observed winds, model description and simulated tracer experiments, in *Aspects of Climate Variability in the Pacific and the Western Americas*, *Geophys. Monogr. Ser.*, vol. 55, edited by D. H. Peterson, pp. 237–275, AGU, Washington, D. C., 1989.
- Hein, R., Inverse Modellierung des atmosphärischen Methan-Kreislaufs unter Verwendung eines drei-dimensionalen Modells des Transports und der Chemie der Troposphäre, Ph.D. thesis, Fachbereich Geowiss. der Univ. Hamburg, Hamburg, Germany, 1994.
- Hein, R., P. J. Crutzen, and M. Heimann, An inverse modeling approach to investigate the global atmospheric methane cycle, *Global Biogeochem. Cycles*, *11*, 43–76, 1997.
- Hertel, O., R. Berkowicz, J. Christensen, and O. Hov, Test of two numerical schemes for use in atmospheric transport-chemistry models, *Atmos. Environ., Part A*, *27*, 2591–2611, 1993.
- Houweling, S., F. J. Dentener, and J. Lelieveld, The impact of non-methane hydrocarbon compounds on tropospheric photochemistry, *J. Geophys. Res.*, *103*, 10,673–10,696, 1998.
- Huang, Y., R. L. Sass, and F. M. Fisher, Methane emissions from Texas rice paddy soils, 1, Quantative multi-year dependence of CH<sub>4</sub> emissions on soil, cultivar and grain yield, *Global Change Biol.*, *3*, 479–489, 1997.
- IPCC, *Climate Change: The IPCC Scientific Assessment*, Edited by J. T. Houghton et al., Cambridge Univ. Press, New York, 1990.

- IPCC, Radiative forcing of climate change and an evaluation of the IPCC IS92 emission scenarios, in *Climate Change 1994*, edited by J. T. Houghton et al., Cambridge Univ. Press, New York, 1994.
- Kaminski, T., M. Heimann, and R. Giering, Sensitivity of the seasonal cycle of CO<sub>2</sub> at remote monitoring stations with respect to seasonal surface exchange fluxes determined with the adjoint of an atmospheric transport model, *Phys. Chem. Earth*, *21*, 457–462, 1996.
- Kaminski, T., M. Heimann, and R. Giering, A coarse grid three-dimensional global inverse model of the atmospheric transport, 1, Adjoint model and Jacobian matrix, *J. Geophys. Res.*, 1999a, in press.
- Kaminski, T., M. Heimann, and R. Giering, A coarse grid three-dimensional global inverse model of the atmospheric transport, 2, Inversion of the transport of CO<sub>2</sub> in the 1980s, *J. Geophys. Res.*, 1999b, in press.
- Kanakidou, M., F. J. Dentener, and P. J. Crutzen, A global three-dimensional study of the fate of HCFCs and HFC-134a in the troposphere, *J. Geophys. Res.*, *100*, 18,781–18,802, 1995.
- Keeling, C. D., S. C. Piper, and M. Heimann, A three dimensional model of the atmospheric CO<sub>2</sub> transport based on observed winds, 4, mean annual gradients and interannual variations, in *Aspects of Climate Variability in the Pacific and the Western Americas*, *Geophys. Monogr. Ser.*, vol. 55, edited by D. H. Peterson, pp. 305–363, AGU, Washington, D. C., 1989.
- Kern, J. S., D. Bachelet, and M. Tolg, Organic matter inputs and methane emissions from soils in major rice growing regions of China, in *Soils and Global Change: advances in Soil Science*, edited by R. Lal, E. Levine, J. Kimble, and B. A. Stewart, CRC Lewis Publishers, New York, 1995.
- Kern, J. S., Z. Gong, G. Zhang, H. Zhuo, and G. Luo, Spatial analysis of methane emissions from paddy soils in China and the potential for emissions reduction, *Nutrient Cycl. Agro-Ecosyst.*, *49*, 181–195, 1997.
- Kreileman, G. J. J., Documentation of a geographically explicit dynamic carbon cycle model, *RIVM report*, Natl. Inst. for Public Health and the Environ. (RIVM), Bilthoven, The Netherlands, 1996.

- Krol, M., P. J. van Leeuwen, and J. Lelieveld, Global OH trend inferred from methylchloroform measurements, *J. Geophys. Res.*, *103*, 10,697–10,711, 1998.
- Lacroix, A. V., Unaccounted-for sources of fossil and isotopically-enriched methane and their contribution to the emissions inventory: A review and synthesis, *Chemosphere*, *26*, 507–557, 1993.
- Lambert, G., and S. Schmidt, Reevaluation of the oceanic flux of methane: Uncertainties and long term variations, *Chemosphere*, *26*, 579–589, 1993.
- Law, R., and I. Simmonds, The sensitivity of deduced CO<sub>2</sub> sources and sinks to variations in transport and imposed surface concentrations, *Tellus, Ser. B*, *48*, 613–625, 1996.
- Lelieveld, J., P. J. Crutzen, and F. J. Dentener, Changing concentration, lifetime and climate forcing of atmospheric methane, *Tellus, Ser. B*, *50*, 128–150, 1998.
- Louis, J. F., A parametric model of vertical eddy fluxes in the atmosphere, *Boundary Layer Meteorol.*, *17*, 187–202, 1979.
- Matthews, E., Global vegetation and land use: New high-resolution data bases for climate studies, *J. Clim. Appl. Meteorol.*, *22*, 474–487, 1983.
- Matthews, E., and I. Fung, Methane emissions from natural wetlands: Global distribution, area, and environmental characteristics of sources, *Global Biogeochem. Cycles*, *1*, 61–86, 1987.
- Matthews, E., I. Fung, and J. Lerner, Methane emission from rice cultivation: Geographic and seasonal distribution of cultivated areas and emissions, *Global Biogeochem. Cycles*, *5*, 3–24, 1991.
- Midgley, P. M., The production and release to the atmosphere of 1,1,1-trichloroethane (methyl chloroform), *Atmos. Environ.*, *23*, 2663–2665, 1989.
- Midgley, P. M., and A. McCulloch, The production and global distribution of emissions to the atmosphere of 1,1,1-trichloroethane (methyl chloroform), *Atmos. Environ.*, *29*, 1601–1608, 1995.
- Mulquiney, J. E., and J. A. Norton, A new inverse method for trace gas flux estimation: State-space model identification and constraints, *J. Geophys. Res.*, *103*, 1417–1427, 1998.

- Mulquiney, J. E., J. A. Taylor, A. J. Jakeman, J. P. Norton, and R. G. Prinn, A new inverse method for trace gas flux estimation: Application to tropospheric  $\text{CFCl}_3$  fluxes, *J. Geophys. Res.*, *103*, 1429–1442, 1998.
- Olivier, J. G. J., et al., Description of EDGAR version 2.0: A set of global emission inventories of greenhouse gases and ozone depleting substances for all anthropogenic and most natural sources on a per country basis on  $1^\circ \times 1^\circ$  grid, *RIVM Rep. 771060 002/TNO MEP Rep. R96/119*, Natl. Inst. for Public Health and the Environ., Bilthoven, The Netherlands, 1996.
- Olson, J. S., J. A. Watts, and L. J. Allison, Carbon in live vegetation of major world ecosystems, *Ornl 5862*, Oak Ridge Lab., Oak Ridge, Tenn., 1983.
- Plumb, R. A., and X. Zheng, Source determination from trace gas observations: An orthogonal function approach and results for long-lived gases with surface sources, *J. Geophys. Res.*, *101*, 18,569–18,585, 1996.
- Prather, M., M. McElroy, S. Wofsy, G. Russell, and D. Rind, Chemistry of the global troposphere: Fluorocarbons as tracers of air motion, *J. Geophys. Res.*, *92*, 6579–6613, 1987.
- Prinn, R. G., R. F. Weiss, B. R. Miller, F. N. Alyea, D. M. Cunnold, D. E. Hartley, P. B. Fraser, and P. G. Simmonds, *Global weighted-average concentration and trend of OH based on 15 years of ALE/GAGE  $\text{CH}_3\text{CCl}_3$  data*, paper presented at Joint Meeting on Global Atmospheric Chemistry, Int. Assoc. of Meteorol. and Atmos. Phys., Fuji-Yoshida, Jpn., 1994.
- Prinn, R. G., R. F. Weiss, B. R. Miller, J. Huang, F. N. Alyea, D. M. Cunnold, P. B. Fraser, D. E. Hartley, and P. G. Simmonds, Atmospheric trends and lifetime of trichloro-ethane and global average hydroxyl radical concentrations based on 1978–1994 ALE/GAGE measurements, *Science*, *269*, 187–192, 1995.
- Prinn, R. G., et al., Global average concentration and trend for hydroxyl radical deduction from ALE/GAGE trichloroethane (methyl chloroform) data for 1978-1990, *J. Geophys. Res.*, *97*, 2445–2461, 1992.
- Ramonet, M., and P. Monfray,  $\text{CO}_2$  baseline concept in 3-D atmospheric transport models, *Tellus, Ser. B*, *48*, 502–520, 1996.

- Rayner, P. J., I. G. Enting, and C. M. Trudinger, Optimizing the CO<sub>2</sub> observing network for constraining sources and sinks, *Tellus, Ser. B*, 48, 433–444, 1996.
- Russell, G., and J. Lerner, A new finite-differencing scheme for the tracer transport equation, *J. Appl. Meteorol.*, 20, 1483–1498, 1981.
- Sanderson, M. G., Biomass of termites and their emissions of methane and carbon dioxide: A global database, *Global Biogeochem. Cycles*, 10, 543–557, 1996.
- Tans, P. P., A note on isotopic ratios and the global atmospheric methane budget, *Global Biogeochem. Cycles*, 11, 77–81, 1997.
- Tarantola, A., *Inverse Problem Theory, Methods for Data Fitting and Model Parameter Estimation*, Elsevier, New York, 1987.
- Tiedke, M., A comprehensive mass flux scheme for cumulus parameterization in large-scale models, *Mon. Weather Rev.*, 117, 1779–1800, 1989.
- Trampert, J., and R. Snieder, Model estimations biased by truncated expansions: Possible artifacts in seismic tomography, *Science*, 271, 1257–1260, 1996.
- van Minnen, J. G., K. Klein Goldewijk, and R. Leemans, The importance of feedback processes and vegetation transition in the terrestrial carbon cycle, *J. Biogeogr.*, 22, 805–814, 1996.
- Warneck, P., Chemistry of the Natural Atmosphere, *Int. Geophys. Ser.*, vol. 41, p. 757, Acad. Press, San Diego, Calif., 1988.
- Yao, H., Y. B. Zhuang, and Z. L. Chen, Estimation of methane emission from rice paddies in mainland China, *Global Biogeochem. Cycles*, 10, 641–649, 1996.
- Yienger, J. J., and H. Levy, Empirical model of global soil-biogenic NO<sub>x</sub> emissions, *J. Geophys. Res.*, 100, 11,447–11,464, 1995.

---

F. J. Dentener, S. Houweling, and J. Lelieveld, Institute for Marine and Atmospheric Research Utrecht, Utrecht University, Princetonplein 5, 3584 CC Utrecht, The Netherlands. (f.j.dentener@phys.uu.nl; s.houweling@phys.uu.nl; j.lelieveld@phys.uu.nl)

M. Heimann, Max Planck Institut für Biogeochemie, postfach 100146, D-07745, Jena, Germany (martin.heimann@bgc-jena.mpg.de)

T. Kaminski, Max Planck Institut für Meteorologie, Bundesstr. 55, D-20146, Hamburg, Germany (kaminski@dkrz.de)

Received March 17, 1999; revised June 10, 1999; accepted June 15, 1999.

---

This manuscript was prepared with AGU's  $\text{\LaTeX}$  macros v4, with the extension package 'AGU++' by P. W. Daly, version 1.5d from 1997/04/28.

## Figure Captions

**Figure 1.** Comparison of modeled 1,1,1-trichloroethane ( $\text{CH}_3\text{CCl}_3$ ) concentrations to measurements at the Atmospheric Lifetime Experiment (ALE)/ Global Atmospheric Gases Experiment (GAGE) stations. Solid lines are optimized OH fields; dashed lines are original OH fields; and squares are monthly mean measurements. Error bars represent the  $1\sigma$  interval of the measurements.

**Figure 2.** Estimated surface fluxes of methane for (left) January and (right) July: (a) a priori, (b) a posteriori, and (c) difference a posteriori minus a priori.

**Figure 3.** As Figure 2 for annual means.

**Figure 4.** Comparison of simulated concentrations to measurements. Dashed lines represent simulations based on a priori fluxes; solid lines represent simulations based on a posteriori fluxes; and squares represent monthly means of observations. Error bars represent the  $1\sigma$  interval of the measurements. The offset of the a priori data has been adjusted according to the offset at the South Pole.

**Figure 5.** Observed and simulated latitudinal methane concentration gradients (representing annual means). Squares represent simulations based a priori fluxes; triangles represent simulations based on a posteriori fluxes; and solid circles represent measurements. The offset in the a priori data has been adjusted according to the offset at the South Pole.

**Figure 6.** Reduction in surface flux uncertainty gained by the inversion ( $1 - \sigma_{\text{a posteriori}}/\sigma_{\text{a priori}}$ ): (a) January, (b) July, (c) annual mean.

**Figure 7.** (a) A posteriori uncertainty covariances between the July flux for a grid in Brazil and all remaining fluxes for July and (b) the same as Figure 7a but for a grid in China. Covariances are expressed in units of the corresponding (Brazilian or Chinese) variances. (Consequently, these Chinese and Brazilian grids both have a value of 1.)

**Figure 8.** Comparison between simulated and observed concentrations. Measurements at these locations have been excluded from the inversion. Dashed lines represent a priori; solid lines represent a posteriori; and squares represent measurements. Error bars represent  $1\sigma$  interval of the measurements.

**Figure 9.** Seasonal cycles in the estimated fluxes for four regions. Solid lines are uncorrelated fluxes; dashed lines are time-orrelated fluxes (see text); and dotted lines are a priori fluxes.

**Figure 10.** Spatial correlation: difference between a posteriori and a priori (a posteriori minus a priori) surface flux estimates for (a) January , (b) July, and (c) annual mean.

## Tables

**Table 1.** Measurement Stations

Station Code	Location	Coordinates		
		Latitude	Longitude	Altitude, m
ALT*	Alert	82°27'N	62°31'W	210
ASC*	Ascension Island	7°55'S	14°25'W	54
BAL	Baltic Sea	55°30'N	16°40'E	7
BME	Bermuda East	32°22'N	64°39'W	30
BMW	Bermuda West	32°16'N	65°53'W	30
BRW*	Barrow	71°19'N	156°36'W	11
CBA	Cold Bay	55°12'N	162°43'W	25
CGO*	Cape Grim	40°41'S	144°41'E	94
CMO	Cape Meares	45°29'N	123°58'W	30
GMI*	Guam	13°26'N	144°47'E	2
GOZ	Gozo	36°03'N	14°11'E	30
ICE	Heimaey	63°15'N	20°09'W	100
ITN	Grifton	35°21'N	77°23'W	505
IZO	Tenerife	28°18'N	16°29'W	2300
KEY	Key Biscayne	25°40'N	80°12'W	3
KUM*	Cape Kumukahi	19°31'N	154°49'W	3
MBC*	Mould Bay	76°15'N	119°21'W	58
MHT	Mace Head	53°20'N	9°54'W	25
MID*	Midway	28°13'N	177°22'W	4
MLO*	Mauna Loa	19°32'N	155°35'W	3397

**Table 1.** (continued)

Station Code	Location	Coordinates		
		Latitude	Longitude	Altitude, m
NWR	Niwot Ridge	40°03'N	105°35'W	3475
P01*	Pacific cruise	10°00'S	168°36'W	0
P02*	Pacific cruise	15°00'S	175°42'W	0
P03*	Pacific cruise	25°00'S	178°00'E	0
P04*	Pacific cruise	30°00'S	177°06'E	0
PSA*	Palmer Station	64°55'S	64°00'W	10
QPC	Qinghai Province	36°16'N	100°55'E	3810
RPB*	Barbados	13°10'N	59°26'W	3
SC1	South China Sea cruise	3°00'N	105°12'E	0
SC2	South China Sea cruise	6°00'N	107°18'E	0
SC3	South China Sea cruise	9°00'N	109°24'E	0
SC4	South China Sea cruise	12°00'N	111°00'E	0
SC5	South China Sea cruise	15°00'N	112°18'E	0
SC6	South China Sea cruise	18°00'N	113°18'E	0
SC7	South China Sea cruise	21°00'N	114°00'E	0
SEY*	Seychelles	4°40'S	55°10'E	3
SHM*	Shemya Island	52°43'N	174°06'E	40
SMO*	American Samoa	14°15'S	170°34'W	42

**Table 1.** (continued)

Station Code	Location	Coordinates		
		Latitude	Longitude	Altitude, m
SPO*	South Pole	89°59'S	24°48'W	2810
STM*	Ocean Station "M"	66°00'N	2°00'E	7
SYO*	Syowa	69°00'S	39°35'E	11
TAP	Tae-ahn Peninsula	36°44'N	126°08'E	20
UTA	Utah	39°54'N	113°43'W	1320
UUM	Ulaan Uul	44°27'N	111°06'E	914
ZEP	Ny-Alesund	78°54'N	11°53'E	475

\*Station is used to derive the global mean trend.

**Table 2.** A Priori CH<sub>4</sub> Fluxes and Uncertainties

Process	Annual Total	Uncertainty <sup>a</sup>	Seasonality	Reference <sup>b,c</sup>
<i>Anthropogenic Surface Fluxes</i>				
Oil/gas production	51	± 30	...	OL(1,3)
Coal mining	38	± 15	...	OL(1,3)
Landfills	48	± 20	...	OL(1,3)
Domestic ruminants	93	± 35	...	OL(1,3)
Biomass burning	40	± 30	part of the dry season	LE(1), OL(3), H91(4)
Rice agriculture	80	± 50	dependent on the growing season	LE(1), M91(3,4)
Other sources <sup>d</sup>	20	± 16	...	OL(1,3)
<i>Natural Surface Fluxes</i>				
Tropical wetlands	91	± 26	...	LE(1), M87(3)
Boreal/arctic wetlands	54	± 15	temperature dependent	LE(1), M87(3), RH(4)
Termites	20	± 20	...	LE(1), SA(3)
Oceans	15	± 10	...	LE(1), PS(3)
Volcanoes	3.5	± 3	...	LA(1), PS(3)
Wild animals	5	± 5	...	LE(1), PS(3)
Soil oxidation	-30	± 15	...	LE(1), FU(3)
Total	528	± 90		

Fluxes and uncertainties in Tg(CH<sub>4</sub>) yr<sup>-1</sup>.

<sup>a</sup>A 95% uncertainty interval ( $\pm 2\sigma$ ) is used.

<sup>b</sup>References are 1 annual and global flux total; 2 uncertainty in 1 (*Lelieveld et al.* [1998] if not stated explicitly); 3 spatial distribution; and 4 seasonality.

<sup>c</sup>References are OL, *Olivier et al.* [1996]; CR, *Crutzen* [1995]; LE, *Lelieveld et al.* [1998]; H91, *Hao et al.* [1991]; M91, *Matthews et al.* [1991]; M87, *Matthews and Fung* [1987]; RH, *Hein et al.* [1997]; SA, *Sanderson* [1996]; LA, *Lacroix* [1993]; FU, *Fung et al.* [1991]; and PS, present study (see text).

<sup>d</sup>Other sources are the sum of fossil fuel and domestic biofuel combustion, and industrial production of iron, steel, and chemicals.

**Table 3.** Standard Scenario Integrated CH<sub>4</sub> Fluxes and Uncertainties

	A priori		A posteriori	
	Mean	Uncertainty <sup>a</sup>	Mean	Uncertainty <sup>a</sup>
Surface flux				
Globe	528	± 90	505	± 24
Northern Hemisphere (NH)	405	± 81	340	± 19
Southern Hemisphere (SH)	123	± 40	165	± 18
Tropospheric OH				
Tropospheric OH	485	± 25	451	± 22
Stratospheric loss				
Stratospheric loss	40	± 10	37	± 9.7
Trend				
Trend	3	± 94	18	± 7
$c_0$				
$c_0$	1.696	... <sup>b</sup>	1.694	± 0.009

Fluxes and uncertainties are in Tg(CH<sub>4</sub>) yr<sup>-1</sup>.

<sup>a</sup>A 95% uncertainty interval ( $\pm 2\sigma$ ) is used.

<sup>b</sup>Initial methane concentration is in ppmv (see (3)). Uncertainty in  $c_0$  is set to a high value.

**Table 4.** Uncertainty Reduction per Station

Global		Local		
Station	Uncertainty Reduction, <sup>a</sup> %	Station	Uncertainty Reduction, %	
1.	SPO	83	QPC	45
2.	SYO	81	TAP	39
3.	P24	75	GMI	39
4.	PSA	74	SC7	32
5.	P25	71	SC5	20
6.	P22	63	SC6	18
7.	CGO	58	SEY	16
8.	ASC	48	UUM	16
9.	SMO	46	SC4	15
10.	MLO	42	SC3	14
11.	P20	37	GOZ	12
12.	GMI	37	MHT	12
13.	QPC	34	IZO	11
14.	MID	34	STM	10
15.	SHM	34	UTA	9
	⋮		⋮	
41.	TAP	13	CMO	2
42.	UTA	13	P25	1
43.	GOZ	13	P24	1
44.	ITN	5	ALT	<0.5

**Table 4.** (continued)

Global		Local	
Station	Uncertainty Reduction, <sup>a</sup> %	Station	Uncertainty Reduction, %
45. BAL	4	SPO	<0.5

<sup>a</sup>Uncertainty reductions are relative to the uncertainty reductions in a standard inversion (see text).

**Table 5.** Sensitivity Tests, Integrated CH<sub>4</sub> Fluxes and Uncertainties

	Globe	NH	SH	Region 1 <sup>a</sup>	Region 2 <sup>b</sup>
	<i>A Priori</i>				
All inversions	528 (±90) <sup>c</sup>	405 (±81)	123 (±40)	111 (±56)	51 (±28)
	<i>A Posteriori</i>				
Standard	505 (±24)	340 (±19)	165 (±18)	77 (±23)	65 (±20)
Time correlation	500 (±23)	338 (±17)	162 (±16)	80 (±20)	65 (±18)
Space correlation	481 (±22)	333 (±15)	148 (±13)	78 (±15)	63 (±14)
Relative uncertainty (600%)	511 (±25)	343 (±21)	169 (±20)	76 (±27)	68 (±25)
Relative uncertainty (100%)	479 (±15)	338 (±9)	142 (±8)	75 (±8)	54 (±6)
OH ratio (NH/SH=2)	516 (±24)	395 (±20)	121 (±17)	103 (±23)	69 (±20)

Fluxes and uncertainties in Tg(CH<sub>4</sub>) yr<sup>-1</sup>.

<sup>a</sup>Region 1 is 75°–135°E, 10°–40°N (southeast Asia).

<sup>b</sup>Region 2 is 5°W–35°E, 15°S–25°N (central Africa).

<sup>c</sup>A 95% uncertainty interval (± 2σ) is used. The a priori uncertainties correspond to the standard scenario only.

**Table 6.** Standard and Low Rice Scenarios, Integrated CH<sub>4</sub> Fluxes, and Uncertainties

Scenario	Globe	NH	SH	Zone <sup>a</sup>	Region <sup>b</sup>
<i>A priori</i>					
Standard	528 (±90)	405 (±81)	123 (±40)	212 (±66)	111 (±56)
Low rice	528 (±77)	384 (±66)	143 (±38)	185 (±47)	74 (±31)
<i>A posteriori</i>					
Standard	505 (±24)	340 (±19)	165 (±18)	169 (±25)	77 (±23)
Low rice	508 (±24)	342 (±18)	166 (±17)	164 (±23)	68 (±18)

Fluxes are in Tg(CH<sub>4</sub>) yr<sup>-1</sup>.

<sup>a</sup>The zonal band is from 10°–40°N.

<sup>b</sup>The region is 75°–135°W, 10°–40°N.

<sup>c</sup>A 95% uncertainty interval ( $\pm 2\sigma$ ) is used.

## Figures

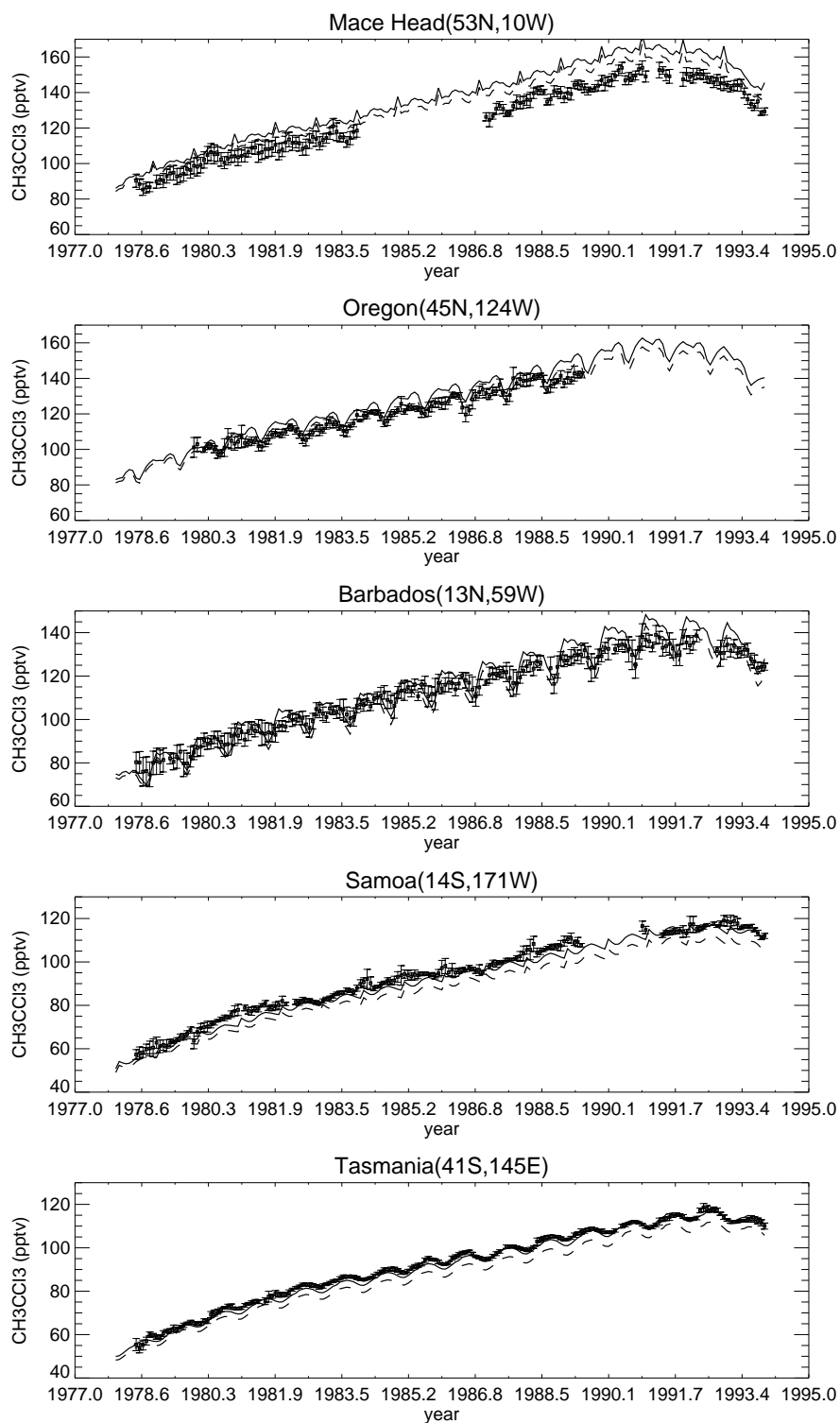


**Figure 1.** Comparison of modeled 1,1,1-trichloroethane ( $\text{CH}_3\text{CCl}_3$ ) concentrations to measurements at the Atmospheric Lifetime Experiment (ALE)/ Global Atmospheric Gases Experiment (GAGE) stations. Solid lines are optimized OH fields; dashed lines are original OH fields; and squares are monthly mean measurements. Error bars represent the  $1\sigma$  interval of the measurements.

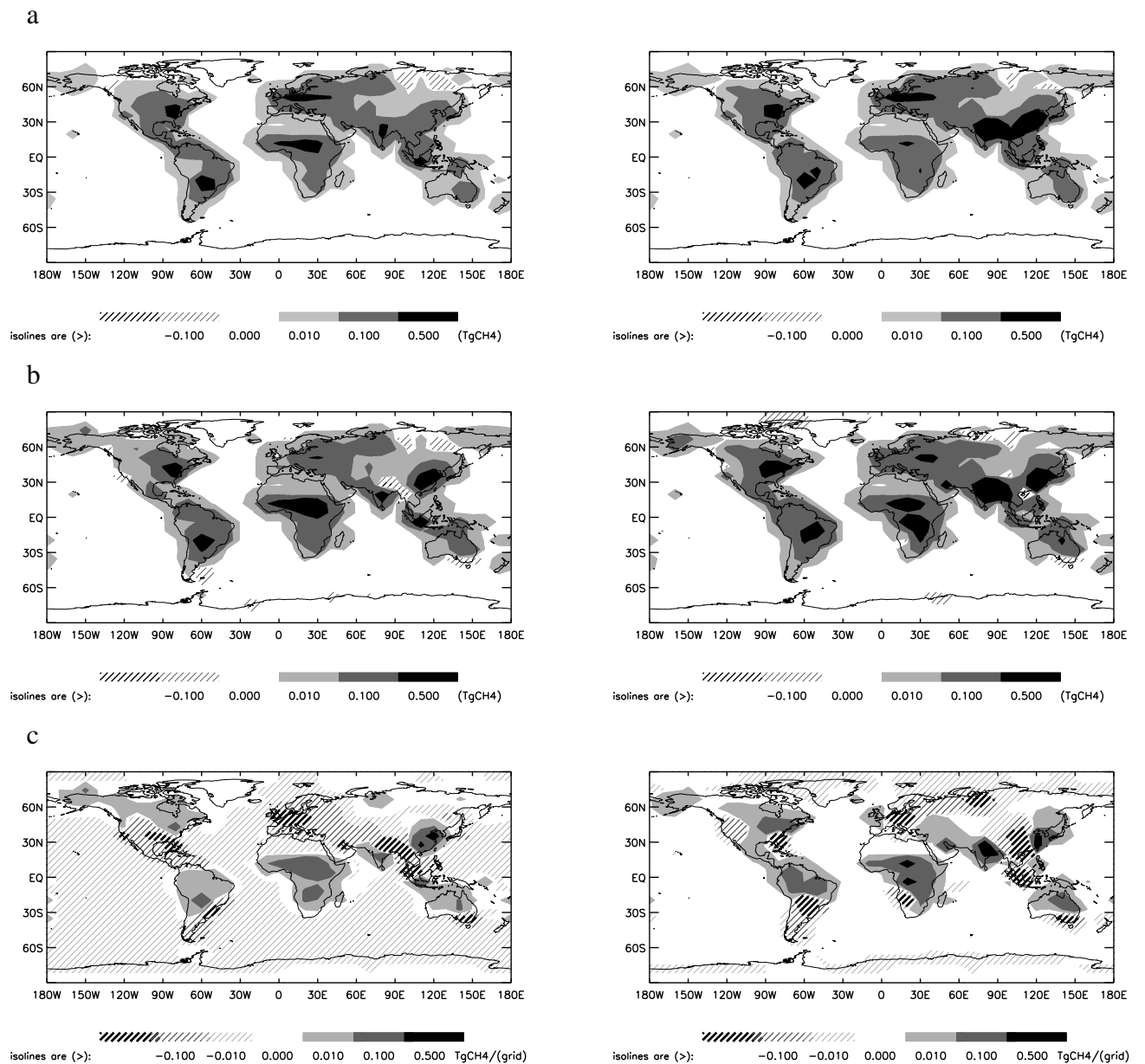


**Figure 2.** Estimated surface fluxes of methane for (left) January and (right) July: (a) a priori, (b) a posteriori, and (c) difference a posteriori minus a priori.

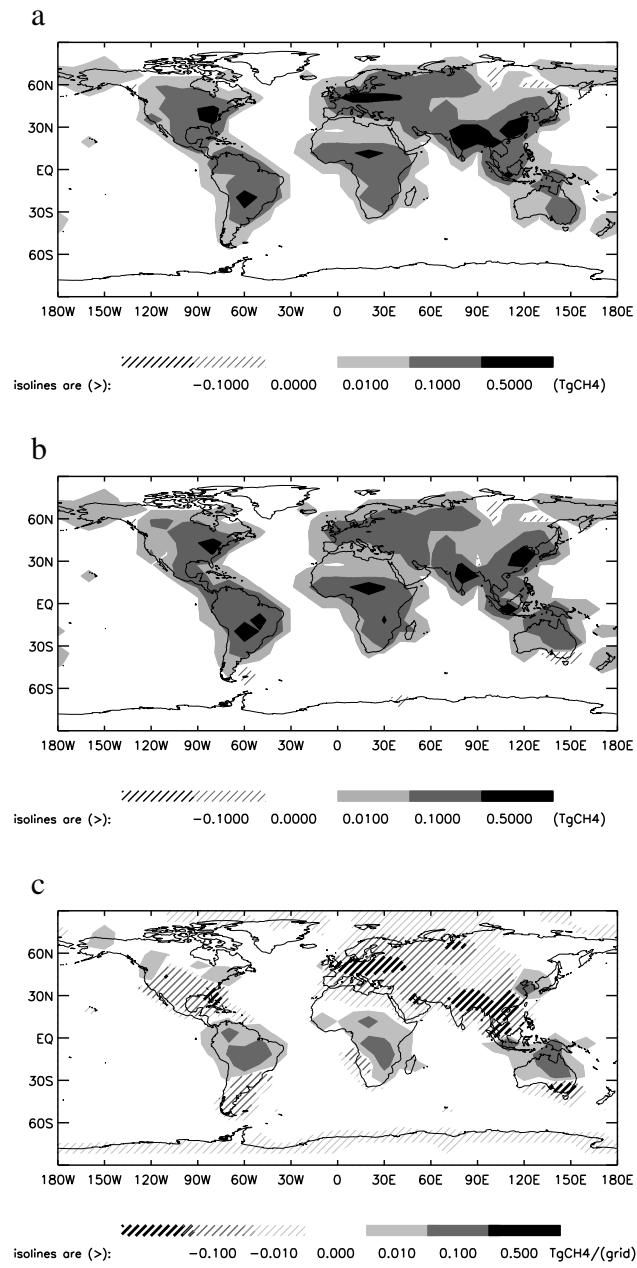


**Figure 3.** As Figure 2 for annual means.

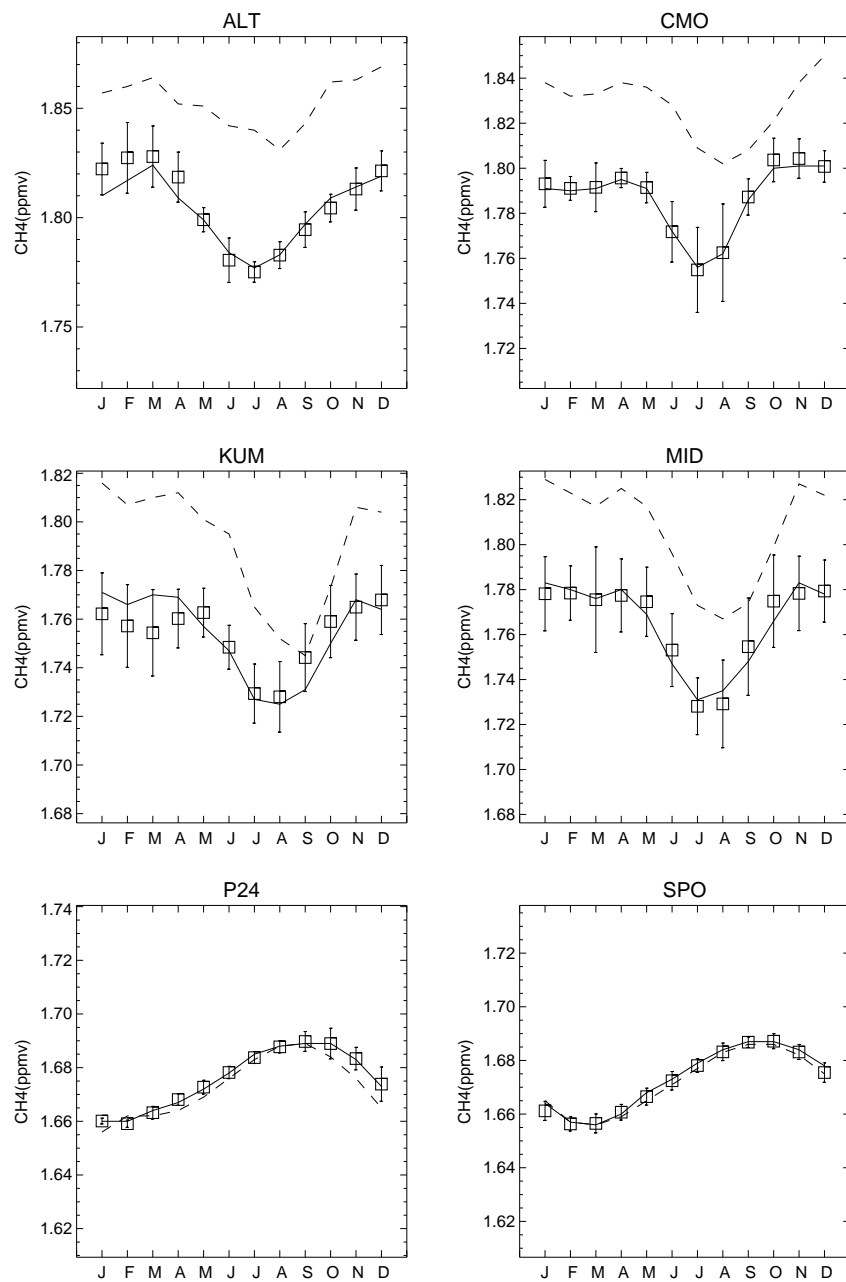


**Figure 4.** Comparison of simulated concentrations to measurements. Dashed lines represent simulations based on a priori fluxes; solid lines represent simulations based on a posteriori fluxes; and squares represent monthly means of observations. Error bars represent the  $1\sigma$  interval of the measurements. The offset of the a priori data has been adjusted according to the offset at the South Pole.

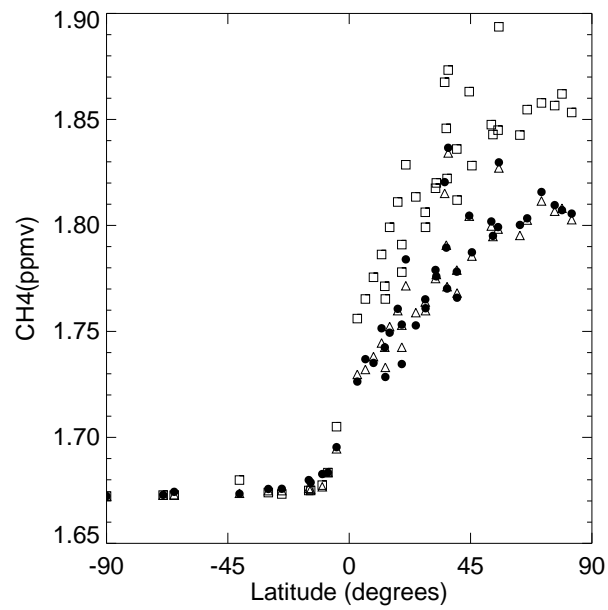


**Figure 5.** Observed and simulated latitudinal methane concentration gradients (representing annual means). Squares represent simulations based a priori fluxes; triangles represent simulations based on a posteriori fluxes; and solid circles represent measurements. The offset in the a priori data has been adjusted according to the offset at the South Pole.

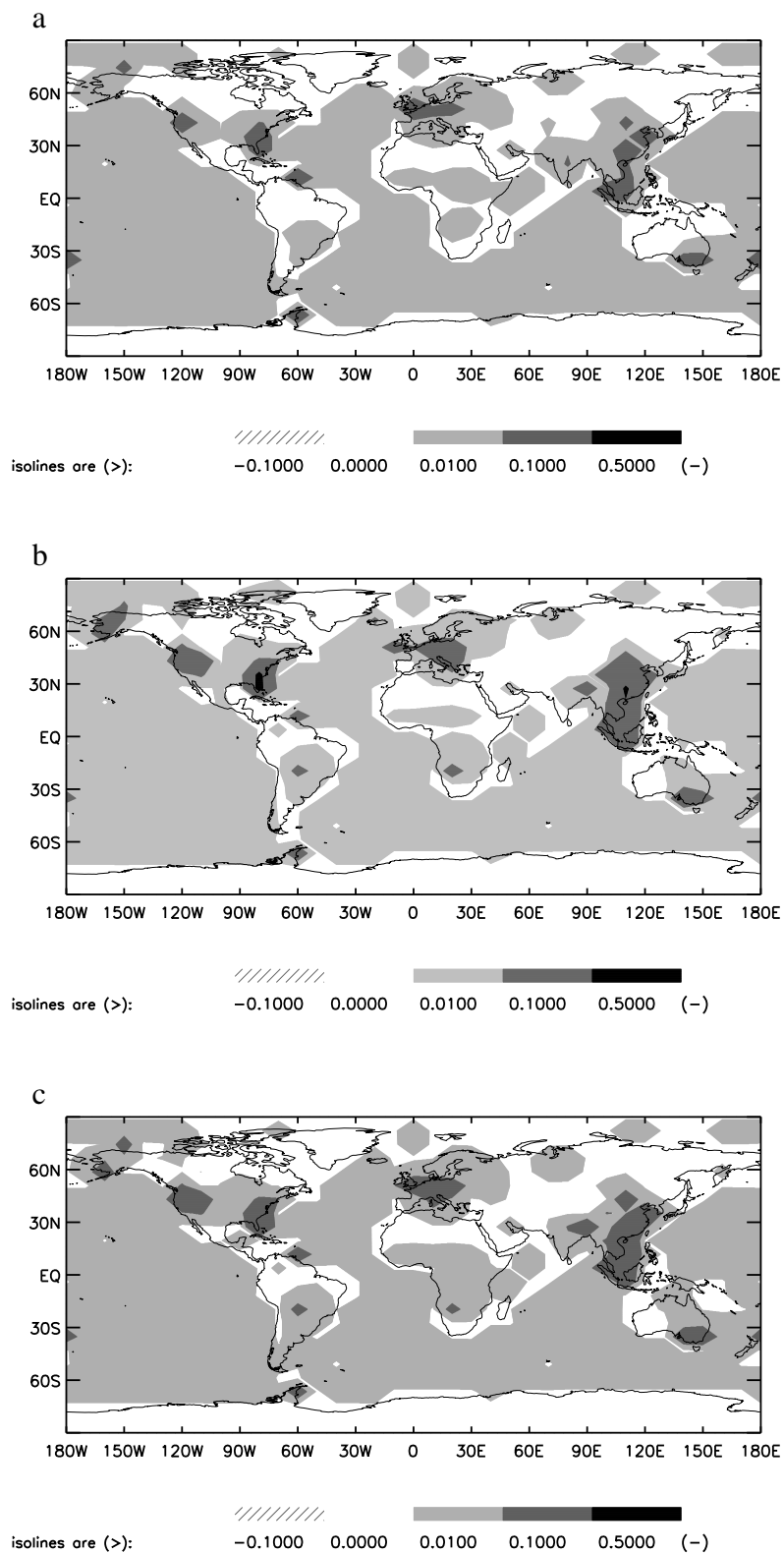


**Figure 6.** Reduction in surface flux uncertainty gained by the inversion ( $1 - \sigma_{\text{posteriori}}/\sigma_{\text{priori}}$ ): (a) January, (b) July, (c) annual mean.

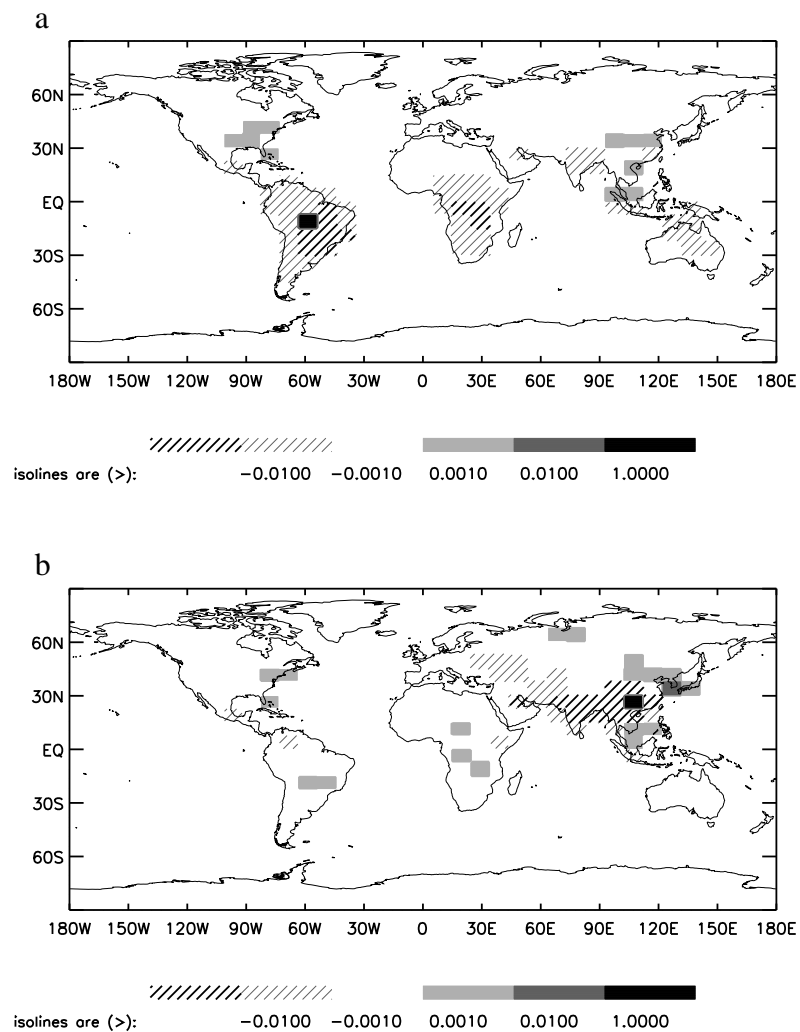


**Figure 7.** (a) A posteriori uncertainty covariances between the July flux for a grid in Brazil and all remaining fluxes for July and (b) the same as Figure 7a but for a grid in China. Covariances are expressed in units of the corresponding (Brazilian or Chinese) variances. (Consequently, these Chinese and Brazilian grids both have a value of 1.)

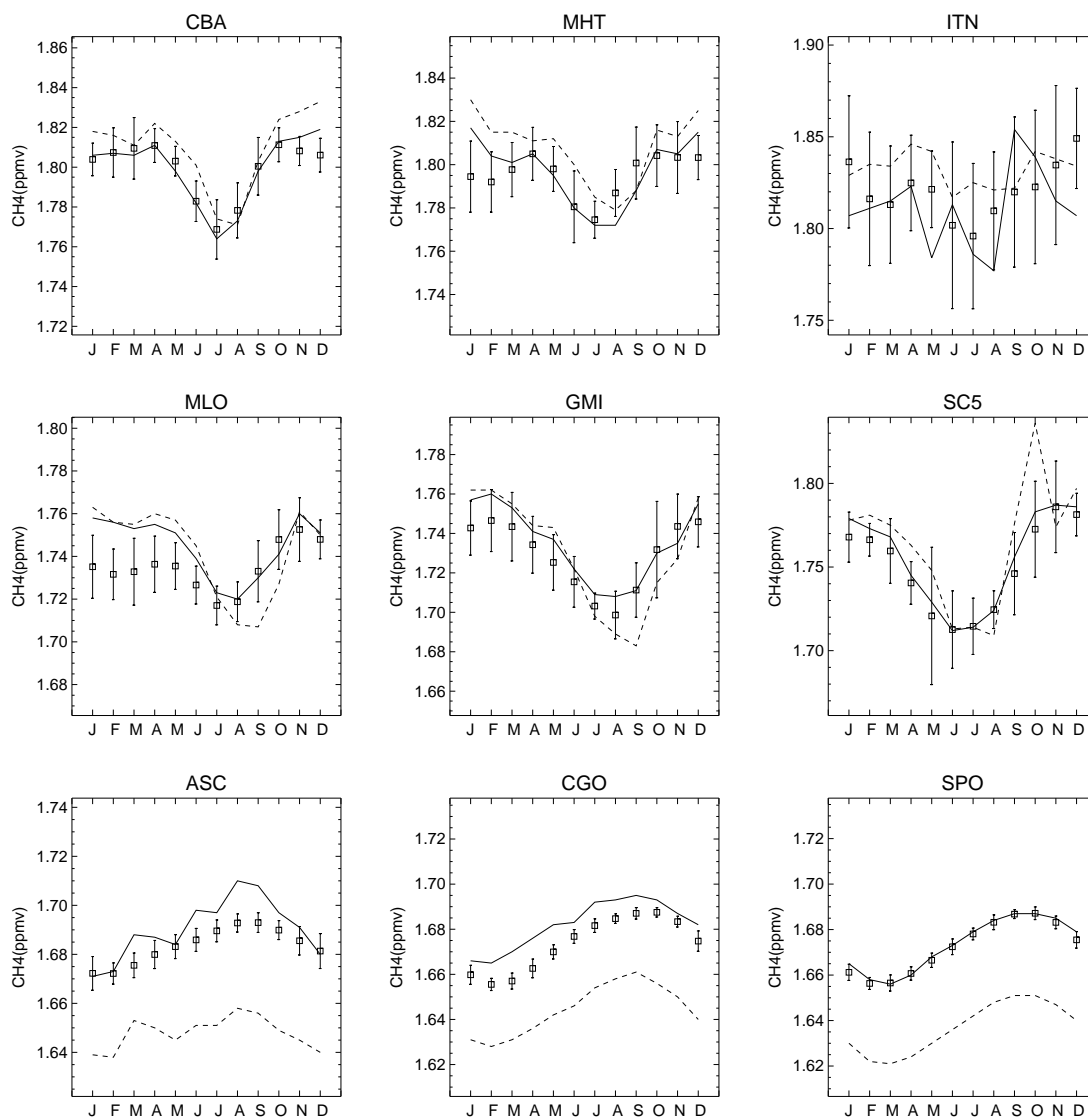


**Figure 8.** Comparison between simulated and observed concentrations. Measurements at these locations have been excluded from the inversion. Dashed lines represent a priori; solid lines represent a posteriori; and squares represent measurements. Error bars represent  $1\sigma$  interval of the measurements.

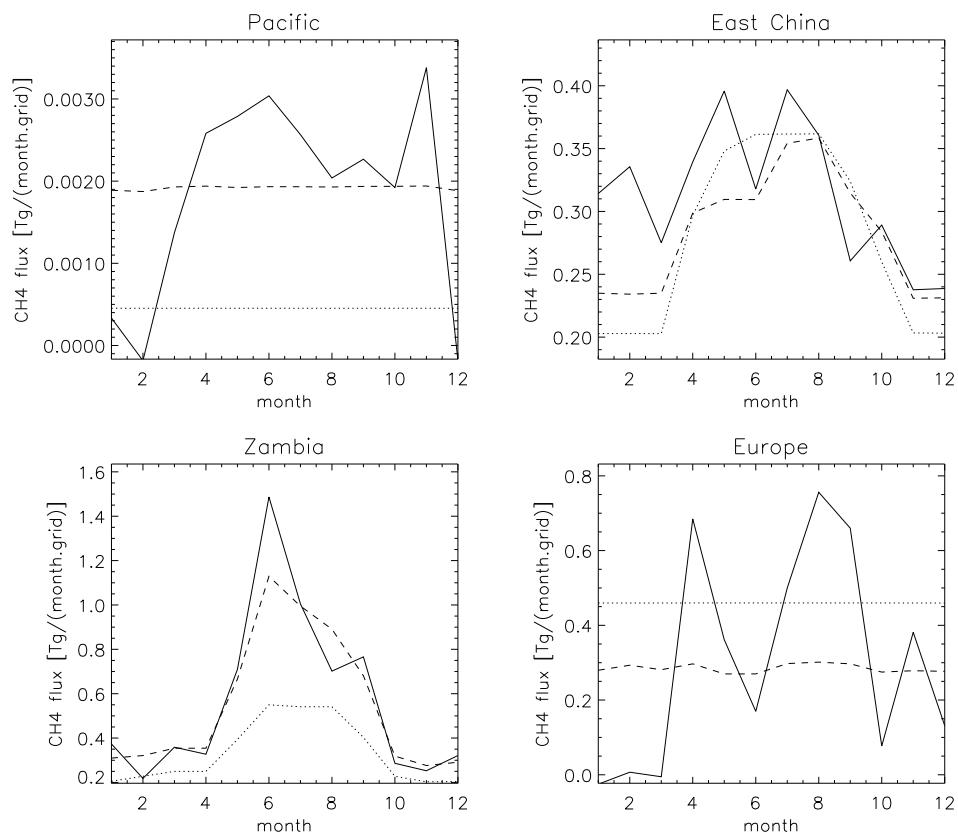


**Figure 9.** Seasonal cycles in the estimated fluxes for four regions. Solid lines are uncorrelated fluxes; dashed lines are time-related fluxes (see text); and dotted lines are a priori fluxes.

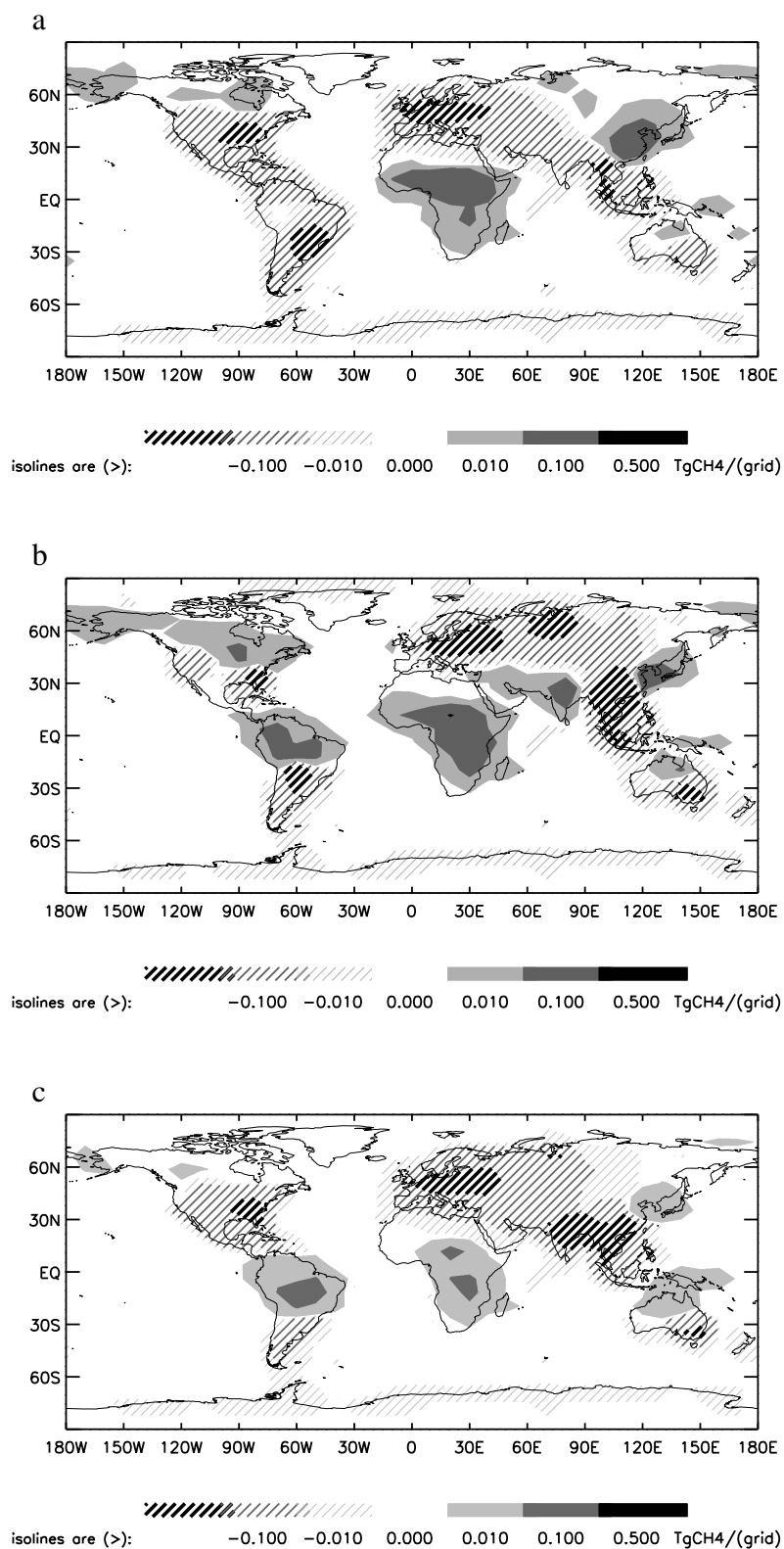


**Figure 10.** Spatial correlation: difference between a posteriori and a priori (a posteriori minus a priori) surface flux estimates for (a) January , (b) July, and (c) annual mean.